UNIVERSITY OF TEXAS ARLINGTON

University of Texas at Arlington McNair Scholars Research Journal

Preparing UTA Students for Careers in Research and Teaching since 1990

MSRJ

UNIVERSITY OF TEXAS AT ARLINGTON
MCNAIR SCHOLARS RESEARCH JOURNAL 2020

Introduction

Papers

Abstracts

MESSAGE

*FROM THE INTERIM
VICE PRESIDENT
FOR RESEARCH*

James P. Grover, Ph.D.

Research is vital to the discovery, invention, and innovation driving our world. It is no coincidence that research is an activity of emphasis at the world's greatest universities. Research is learning at the highest level, and obtaining an education through engagement with research has lifelong benefits through its development of the skills of obtaining evidence, evaluating it and analyzing it, drawing conclusions from it, and communicating these conclusions to others. The University of Texas at Arlington is on an impressive trajectory, joining the ranks of the best research universities in the world. Our vision reflects the way in which education and research come together to meet the needs of our students and our community. As the Dallas-Ft. Worth-Arlington metroplex heads quickly toward joining the ranks of global megacities, the vision highlights our contributions within our region and across the globe.

The McNair Scholars Program plays an important role at UTA in providing experiential learning to prepare promising students from low-income/first-generation or under-represented backgrounds for a successful transition to a PhD program. The program helps students realize their dreams and ambitions by providing the academic support, mentoring and research opportunities necessary to become more competitive in applying for a PhD program and to be well prepared to start their graduate work.

Engaging in research as an undergraduate can give you the preparation needed to be a successful PhD student, if research is a passion for you. Obtaining a PhD degree takes tremendous dedication and persistence, but it is also a tremendous accomplishment, opening a wide range of career opportunities.

The efforts that prepare students to earn a doctoral degree, which the McNair Scholars Program helps accomplish, establish a foundation for a lifetime of discoveries and contributions that will shape our future. This year has been challenging for all who do research, and the persistence of those who successfully completed projects under the circumstances of the Covid-19 pandemic is truly admirable. These students who have demonstrated such resilience and determination will be those whose discoveries improve health, education, and economic growth.

The University of Texas at Arlington is proud to be a supporter of the McNair Scholars Program, which has provided opportunities to so many undergraduates over the last 30 years to help them reach their full academic and professional potential. Those of us who have been privileged to work with McNair Scholars and to witness the transformation from students to scholars are impressed with their sophistication and, as mentors, take great pride in their accomplishments. A special thanks to the faculty who have mentored them. At UTA, we are also proud to have several previous McNair Scholars from other institutions as members of our faculty.

Congratulations Scholars on your acceptance into the program. You have completed impressive work. It is work that portends an exciting future for you and for the promise your future contributions will make.

NOTES

*FROM THE
DIRECTOR*

Joan Reinhardt, Ph.D.

I congratulate McNair Scholars at The University of Texas at Arlington on their conduct and accomplishments during spring and summer of 2020. In challenging times, they have exhibited calm, patience and flexibility, in addition to dedication and self-discipline. Research poses its own challenges, but the obstacles Scholars faced in 2020 have been like those of no other year. I also extend my appreciation to their mentors for the guidance and support they offered to McNair Scholars while themselves grappling with the impact of Covid-19 on and off campus. However, there is hope of soon starting the return to normal. In the meantime, life must go on and many of UTA's McNair Scholars are in the process of applying to graduate school for next fall.

The McNair Scholars program is a national initiative that encourages pursuit of the research doctorate, ideally leading to a career in research and teaching at the university level. It serves undergraduates from first-generation/low-income or underrepresented ethnicities/races. In the 2020 edition of *The University of Texas at Arlington McNair Scholars Research Journal*, seventeen Scholars share with you their research findings, proving yet again what undergraduates at this Research I institution can achieve when offered the chance-- whatever their economic, educational, or ethnic/racial background. Experiential learning such as undergraduate research is often a greatly impactful process for students who choose to engage in it. In the last three decades, many Scholars have participated in this federal TRIO program on their journey to great achievements. Their time at UT Arlington has built a sound foundation for Scholars as they continue on their path to academic and professional success.

In conclusion, I would like to thank Interim President Teik Lim, the Interim Vice President for Research Dr. James Grover, in addition to the Dean of the Library Rebecca Bichel. I would also like to recognize the contributions of those numerous faculty members who over the years have shown vigorous and ongoing support for the program by encouraging undergraduates to apply each year and, especially, by serving on the McNair Selection Committee or as faculty mentors. Thank you all for your contributions!

ABOUT

THE MCNAIR
SCHOLARS PROGRAM

The McNair Scholars Program (officially known as the Ronald E. McNair Post-Baccalaureate Achievement Program) came to the campus of The University of Texas at Arlington in 1990. Created by the U.S. Congress in 1988, it is named after Dr. Ronald E. McNair, who perished with his fellow astronauts on the space shuttle *Challenger* two years earlier. The McNair program endeavors to assist talented undergraduates – either first generation and low-income or underrepresented students – to prepare for graduate study leading to the Ph.D. and the professoriate.

Since its beginning at UT Arlington, the McNair program has encouraged and assisted over 400 scholars in various majors. Currently, it works with 34 students each academic year, providing seminars and classes on topics related to graduate school and the GRE, a May institute to heighten scholars' understanding of the culture of research, and a summer research internship. The program also provides guidance with the graduate school application process and travel funds to participate in conferences and visit prospective graduate programs. UT Arlington McNair graduates have subsequently earned masters and doctorates not only from their alma mater, but also from an impressive array of universities including Harvard, Indiana, Rice, and Southern Methodist, among others.

The McNair Scholars Program enjoys strong support from the UT Arlington administration and greatly benefits from the expertise and enthusiasm of both faculty and staff. Faculty members who serve on the McNair Selection Committee and those who act as mentors to McNair interns deserve special recognition. Members of the 2020-2021 Selection Committee include the following UTA faculty and staff: Dr. Karishma Chatterjee (Communication Studies), Dr. Kenyatta Dawson (Office of Undergraduate Research), Dr. Joe Jackson (the Graduate School), Dr. Qing Lin (Psychology), Dr. Cesar Torres (Computer Science and Engineering), and Dr. Debra Woody (Social Work).

McNair Staff Members

Joan Reinhardt, Ph.D.
Director

Natalie Stephens, M.Ed.
Coordinator

Cheri Counts
Administrative Assistant
(*prior to January 2020*)

Tahanee Mannings
Staff Member
(*beginning October 2020*)

SCHOLARSHIPS

Kathryn A. Head Scholarship Winner

In Summer of 2020 the Kathryn A. Head Scholarship for McNair Scholars was awarded to Jacqueline Baeza-Rubio, a Physics major engaged in program-sponsored research mentored by Dr. Benjamin Jones. Jackie was selected for this award based on her essay, GPA, letters of recommendation, and commitment to pursuing research and the professoriate. The scholarship honors the long and exemplary career of Kathryn A. Head, former director of the McNair Scholars Program and SOAR Learning Services. The scholarship committee includes Natalie Stephens, Undergraduate Research Programs, Coordinator I; Jennifer Luken-Sutton, Student Support Services Director; and Sen Xu, Ph.D., Assistant Professor, Department of Biology and former McNair mentor. We thank our committee members for their commitment to selecting the best candidate for this honor, and we congratulate Jackie on receiving it.

Jacqueline Baeza-Rubio (center, with her family) at the New Scholar Reception in February 2020.

Friends of the UTA Library, Scholarship Winners

The annual Friends of the UT Arlington Library McNair Scholarship was awarded to Michelle Bui (Physics and Math) and Chris McDaniels (Biology) for their McNair research presentations and papers. The scholarship recipients are determined by the excellence of the Scholars' oral research presentations and papers, as assessed by members of the Friends McNair Scholarship Committee: Emilie Algenio, UTA Libraries, Director of Publishing; Brittany Griffiths, UTA Libraries, Publication Specialist; and Yumi Ohira, UTA Libraries, Digital Publishing and Repository Librarian. The annual program research journal includes the four top-ranked papers, as well as abstracts, from spring/summer 2020 McNair research interns. The McNair Scholars Program congratulates its 2020 scholarship winners and thanks the UTA Library for their continued support. Special thanks to Rebecca Bichel, Dean of the UTA Library, and the Friends of the UTA Library.

Michelle Bui (left) and Chris McDaniels (right), the winners of the Friends of the UTA Library Scholarship for McNair Scholars.

COMPARING APPROXIMATE TOTAL CURRENT OF THE DAYSIDE MAGNETOPAUSE TO SOLAR WIND PRESSURE

Michelle X. Bui

Physics and Mathematics Major

Faculty Mentor: Ramon E. Lopez, Ph.D

Department of Physics

ABSTRACT

The solar wind pushes against Earth's magnetic field to form a cavity called the magnetosphere, which contains Earth's dipole field. The solar wind also carries a magnetic field, and the interaction between magnetospheric field and solar wind magnetic field is located at the magnetopause. The magnetopause is the boundary between the interplanetary magnetic field and Earth's dipole field, and its shape and location are dependent upon pressure balance. At the magnetopause, the Chapman-Ferraro current layer flows, balancing the pressure of the solar wind and accounting for the change of the magnetic field across the magnetopause. The total current of the magnetopause fluctuates due to changes in the magnitude of the solar wind magnetic field and the solar wind dynamic pressure. This study observes the approximate total current of the dayside magnetopause and compares it with the value of the solar wind pressure for both positive and negative z-components of the solar wind. Using open-source Python libraries, approximate total current can be calculated and plotted against solar wind dynamic pressure to determine a least-squares fit. Results show similar positive statistical correlations between the total current of the dayside magnetopause to solar wind pressure during periods of northward and southward orientation of interplanetary magnetic field.

Introduction

The magnetopause is a boundary between Earth's magnetic field and surrounding plasma, also known as the magnetosheath. Pressure balance between the magnetosphere and the magnetosheath determines the location of the magnetopause. The shape of the magnetopause depends on interplanetary magnetic field (IMF) conditions, which affect the plasma flow and define the magnetospheric boundary (Sibeck et al. 1991; Lopez and Gonzalez 2017). On the magnetopause, the Chapman-Ferraro current flows and typically produces a force exerted on magnetosheath plasma during high magnetosonic mach number, greater than 6. During instances of low magnetosonic mach number, around 2, force is not exerted at the magnetopause by the currents flowing along the magnetopause; instead, $J \times B$ force is exerted at the bow shock by currents that connect to Region 1 currents. The force and the pressure gradient contribute to acceleration of magnetosheath plasma (Lopez and Gonzalez 2017).

IMF conditions can be separated based on the direction of the z-component of magnetic field (x points toward the sun, y is in the direction of Earth's orbital motion, and z points northward). During southward IMF, magnetic reconnection occurs as the negative B_z magnetic field of the solar wind is pushed into the positive B_z magnetospheric field by the solar wind flow. When magnetic reconnection occurs, solar wind power is deposited into the ionosphere. This deposition drives a current system called Region I, which enters the ionosphere on the dawn and exits the ionosphere on the dusk. This current system weakens the dayside magnetic field strength, which is why the dayside magnetopause must move inward to restore pressure balance between the solar wind flow pressure and the magnetospheric magnetic pressure (Sibeck et al. 1991; Bonde, Lopez, and Wang 2018). When the magnetopause moves inward, this compresses the magnetospheric plasma and magnetic field (Southwood and Kivelson 1990). Part of the Chapman-Ferraro current resides on open field lines; thus, only the net total current will push against solar wind dynamic pressure.

During northward IMF, the positive B_z magnetic field of solar wind is pushed into positive B_z magnetospheric field by the solar wind flow. Since northward IMF is merging into the dipole field, the Chapman-Ferraro current is entirely defined by closed field lines. Magnetic reconnection does not occur at the dayside of the magnetopause; instead, magnetic field of the solar wind wraps around Earth toward the nightside. Change in magnetic field in the dayside is significantly less, and since magnetic reconnection does not occur on the dayside of the magnetosphere, no erosion occurs on the magnetopause. Magnetic reconnection happens instead at high latitudes above the poles of Earth, poleward of the cusp, and solar wind power is deposited directly into the ionosphere (Sibeck et al. 1991). Since the reconnection region is small, the amount of power delivered to the ionosphere is small in comparison with what happens for negative IMF B_z. Separating events of northward and southward IMF is crucial in order to account for differences in reconnection effects.

By analyzing the relationship between dayside magnetopause current and solar wind pressure during northward and southward IMF, electrodynamic relationships can be applied and understood in the context of magnetospheric activity. The magnetosphere can be affected by solar storms such as solar flares, solar energetic particles, and coronal mass ejections (Schwenn 2006; Siscoe 2000). Understanding magnetopause motion and position due to solar activity and verifying electrodynamic relationships is crucial to improving computational models of the magnetosphere. This leads to improvements in space weather prediction models, which forecast the effects of solar storms on Earth.

Methodology

Using data from the Time History of Events and Macroscale Interactions during Substorms (THEMIS) spacecraft, events of the spacecraft crossing the magnetopause can be identified and tabulated for analysis. Magnetopause crossings are easily identified during southward IMF as data clearly reveal an immediate change from negative z-component IMF to positive z-component magnetospheric field. However, magnetopause crossings are more difficult to identify during northward IMF since the both fields are clearly positive in the z-component. Plasma data must be considered in order to determine the approximate time of the magnetopause crossing. The total current of the magnetopause fluctuates due to changes in the magnitude of solar wind magnetic field and the solar wind dynamic pressure; additionally, the location of the magnetopause may vary due to the polarity of the solar wind magnetic field. Total current of the dayside magnetopause can be derived as a function of the three-dimensional curl of the magnetic field and the radial distance of the current layer (Kivelson and Russell 1995). Since change in the x and y components of magnetic field are negligible as the IMF merges with the magnetospheric field, the approximation of total current is primarily dependent on the y-component of current per unit area. After isolating the y-component of current per unit area, current per unit length (J_y) can be derived as a direct relation to change in the z-component of magnetic field (B_z), shown by Equation 1 of Table 1. Total current can then be calculated by taking an approximate total range of the dayside magnetopause. To estimate the length of the dayside magnetopause, an approximate angle of $\pi/2$ can be taken for the arc length (L), where radial distance (n) from Earth is dependent on the location of THEMIS satellites, measured in units of Earth radii (R_E). The length should then be converted from Earth radii to meters to determine the approximate total current. Equation 2 of Table 1 depicts the approximate length of the dayside magnetopause based on the location of a THEMIS satellite at the nose. Current per unit length multiplied by the length of the dayside magnetopause should yield the approximate total current. Thus, the final derivation of the approximate total current of the dayside magnetopause is given by Equation 3 of Table 1, where the result is in units of amperes.

Table 1.

Equations derived to calculate the approximate total current of the dayside magnetopause.

	Equation	Variables
1	$J_y = \dfrac{\Delta B_z}{\mu_0}$	J_y = Current per Unit Length (A/m) B_z = z-component of Magnetic Field (T) μ_0 = Permeability of Free Space
2	$L = \dfrac{\pi}{2} \bullet nR_E$	L = Length (m) n = Distance (R_E) R_E = 1 Earth radii
3	$I = J_y L$	I = Current (A) J_y = Current per Unit Length (A/m) L = Length (m)

Data from nearly fifty southward magnetopause crossings and twenty northward magnetopause crossings were tabulated for analysis of the approximate dayside total current. Solar wind pressure was calculated through compiled OMNIWeb data using solar wind density and velocity data. After gathering from NASA databases, data can be calculated and graphed using Python open-source libraries such as SciPy, NumPy,

and MatPlotLib. A scatterplot seeking trend between solar wind pressure to approximate total current was mapped and analyzed by utilizing the least-squares method of error analysis to deduce a trendline and calculate any statistical correlation between total current and solar wind dynamic pressure (Bevington and Robinson 2003). Standard deviations of the slope and intercept will also be taken into consideration to account for any disparities between the cases of northward and southward IMF.

Example Cases of Northward and Southward Crossings

An example event of THEMIS-A crossing from the magnetosheath to the magnetosphere was observed on March 14, 2014 at approximately 05:20:00 UTC, as shown by Figure 1.
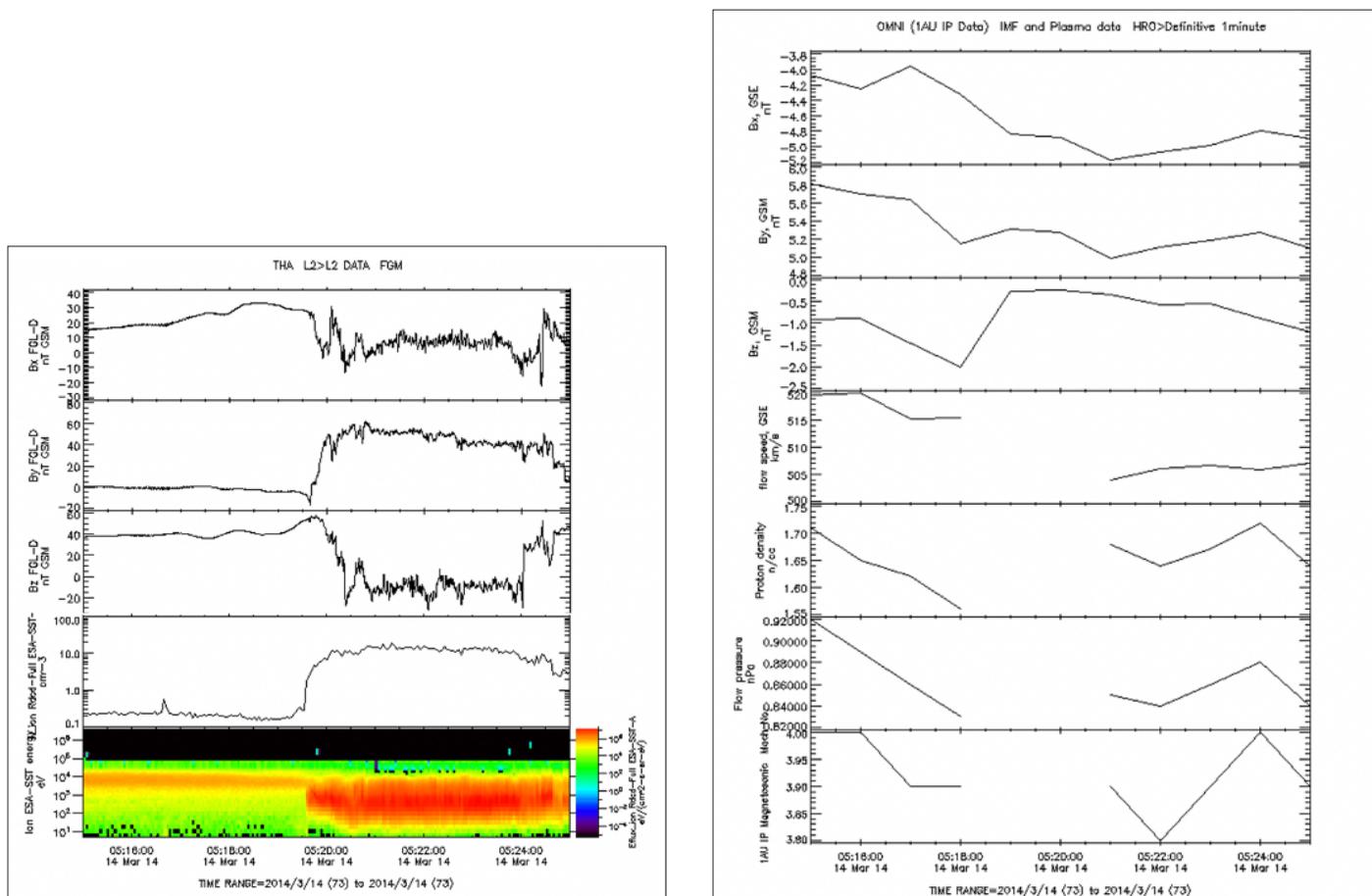
Figure 1 (left). Southward THEMIS-A crossing through the magnetopause on 2014 March 14 at 05:15:00-05:25:00 UTC, shown using magnetic field data and plasma data from the flux-gate magnetometer and the electrostatic analyzer. Figure auto-generated via CDAWeb on 2020 June 1.

Figure 2 (right). Solar wind magnetic field, dynamic pressure, and Magnetosonic Mach number number during the THEMIS-D magnetopause crossing depicted in Figure 1. Figure auto-generated via CDAWeb on 2020 June 1.

THEMIS-A is positioned on the dayside of the magnetosphere at noon at a radial distance of approximately 11 R_E around the nose of the magnetopause. During this event, the z-component of the magnetic field decreased sharply from an average of 38 nT in the magnetosphere to -20 nT in the magnetosheath, revealing a southward IMF in the magnetosheath merging with Earth's northward magnetic field. The crossing occurs at the instance when the z-component of magnetic field data is zero, which is the point of merging between

open and closed field lines. The y-component of the magnetic field increased from roughly 0 nT to 59 nT, which correlates with a positive y-component in solar wind merging with Earth's dipole field and will result in magnetic reconnection poleward of the cusp. The plasma data increases from 0.1 cm^{-3} to 10 cm^{-3}, which is consistent with a transition from the magnetosheath to the magnetosphere. Figure 2 reveals southward solar wind conditions during the period of magnetopause crossing with minimal change in x and y components of IMF. The magnetosonic mach number at crossing is about 3.90, suggesting a typical scenario in which the J × B force on the solar wind plasma is exerted at the magnetopause. Solar wind pressure is an average of 0.86 nPa, which is fairly common during minimal solar activity.

Using the above parameters, the total current per unit length calculated by Equation 1 yielded 0.046 A/m, which will be used as an estimation for the distribution of electric current along the length of the dayside magnetopause. The total dayside magnetopause current calculated by Equation 3 was estimated to be 5.10 x 10^6 A, which is reasonable given that the nose of the magnetopause was about 11 R_E. Southward magnetopause crossing events are expected to yield larger values of approximate total current due to a greater change in magnetic field, as the current is along open and closed field lines.

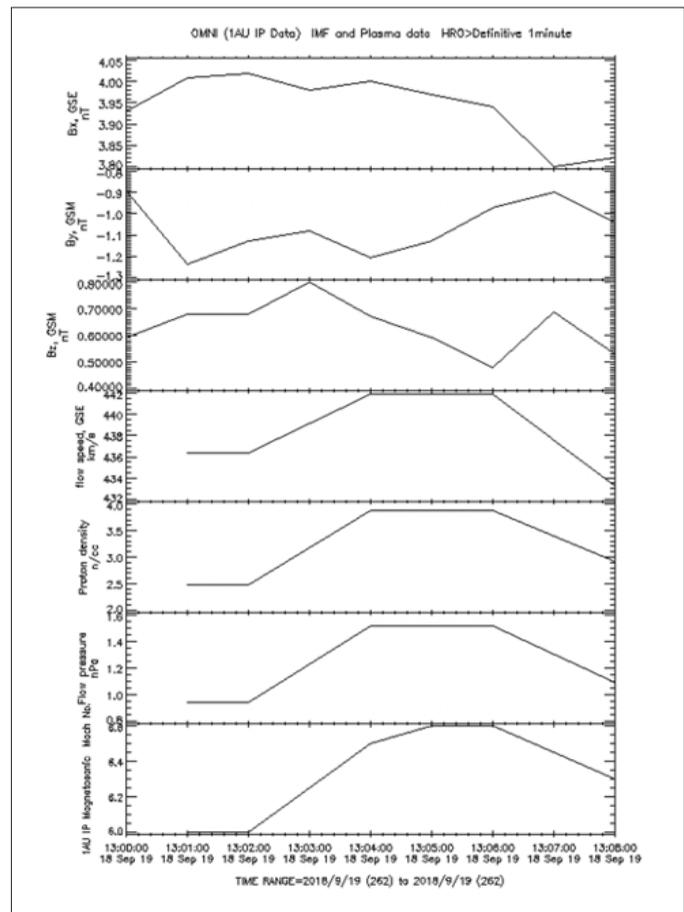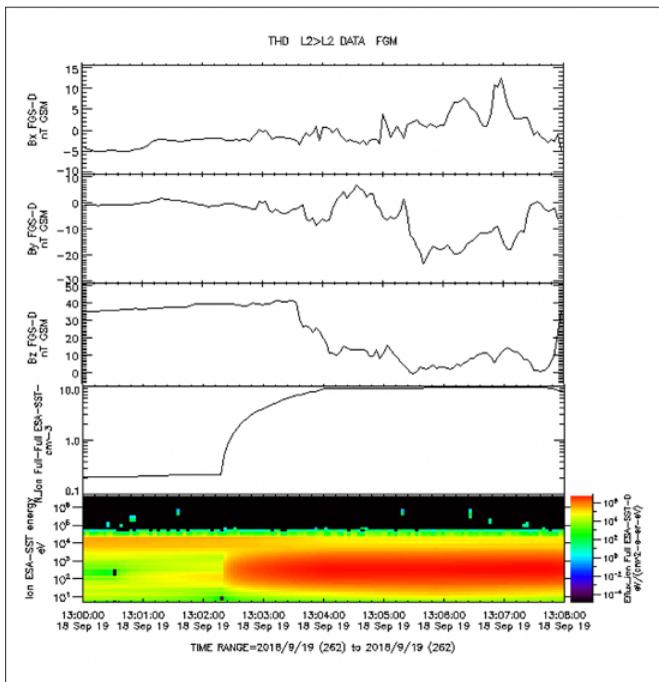

Figure 3 (left). Northward THEMIS-D crossing through the magnetopause on 2018 Sept 19 at 13:00:00-13:10:00 UTC, shown using magnetic field data and plasma data from the flux-gate magnetometer and the electrostatic analyzer. Figure auto-generated via CDAWeb on 2020 June 1.

Figure 4 (right). Solar wind magnetic field, dynamic pressure, and Magnetosonic Mach number number during the THEMIS-D magnetopause crossing depicted in Figure 1. Figure auto-generated via CDAWeb on 2020 June 1.

In contrast, a northward crossing is more unclear since the point of crossing is not at the point of merging between open and closed field lines. As shown in Figure 3, a northward crossing on September 19, 2018 at 13:04 was observed by THEMIS-D at a radial distance of 12.70 RE. The crossing can be identified by the sharp change in plasma density, specifically at the point which plasma density begins at about 0.1 cm^{-3} and reaches its plateau of 10 cm^{-3}, indicating that the THEMIS-D satellite transitions from the magnetosphere to the magnetosheath. The z-component of the magnetic field decreases from approximately 37 nT in the magnetosphere to 7 nT in the magnetosheath, while the y-component of magnetic field decreases from about 0 nT in the dipole field to -18 nT in the magnetosheath. Figure 4 shows northward solar wind conditions with negligible change in the x and y components of solar wind field. The magnetosonic mach number is about 6.50, indicative that magnetic pressure of the magnetosphere is equal to the magnetic pressure of the IMF, driving the $J \times B$ force on the IMF towards the bow shock instead of the magnetopause (Lopez and Gonzalez, 2017). Solar wind pressure is about 1.45 nPa, which is consistent with periods of minimal solar activity.

Calculation through Equation 1 yielded a current per unit length of 0.024 A/m, which is an approximate distribution of the electric current along the arc of the dayside magnetopause. Using Equation 3, approximate total current of the dayside magnetopause current was 3.08 x 10^6 A, which is slightly less than the example southward crossing depicted in Figure 1. During periods of northward magnetopause crossings, values of approximate total current are expected to be lower than values of approximate total current during southward magnetopause crossings since the crossing data only reveals change along closed field lines.

Results
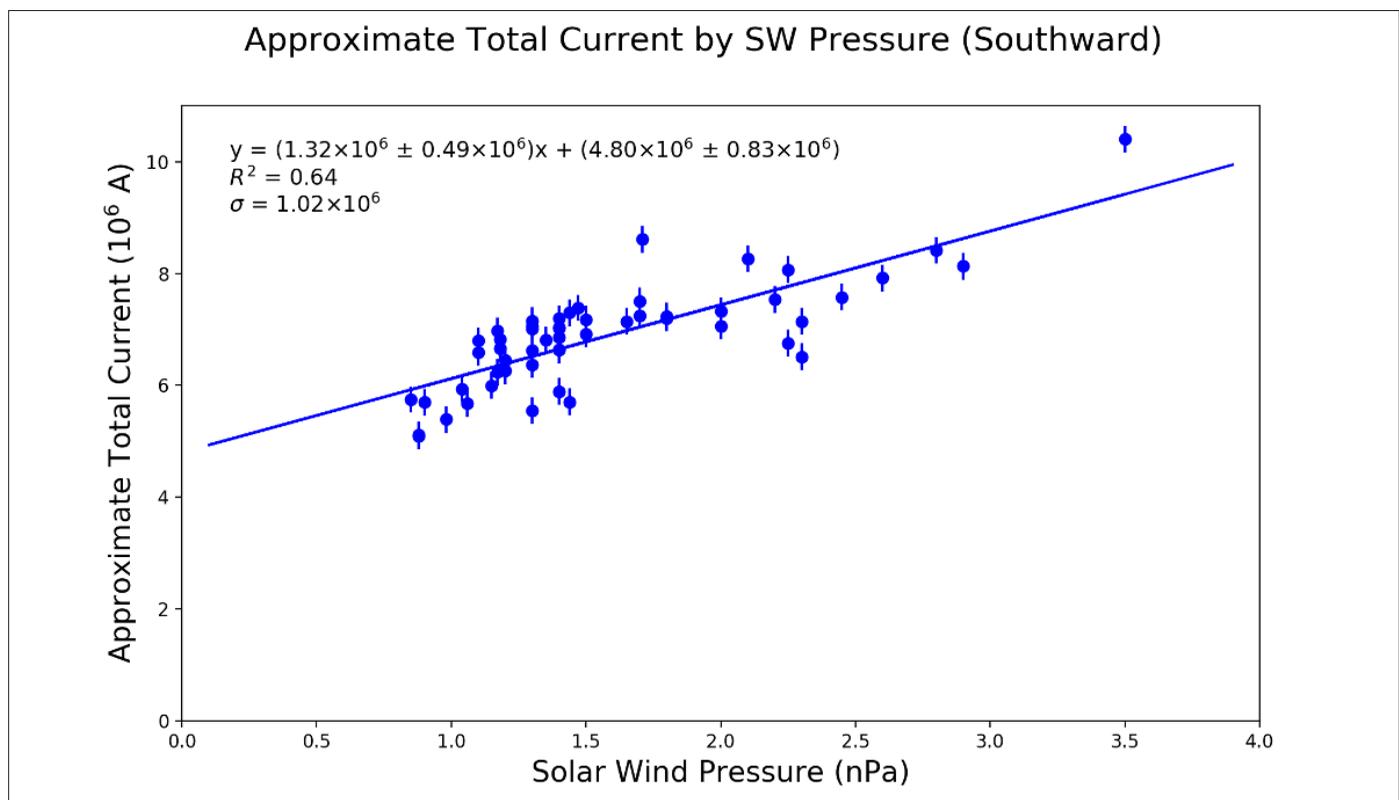
Figure 5. Scatterplot of approximate total current calculated from southward crossings compared to solar wind dynamic pressure at incident of magnetopause crossing events. Figure generated on 2020 June 14 using Python MatPlotLib.

Using about sixty southward magnetopause crossings as shown by Figure 5, OMNIWeb and THEMIS data revealed a positive trend between total current and solar wind dynamic pressure during southward IMF. The electric current increases at about 1.32×10^6 A/nPa with an uncertainty of 0.49×10^6 A/nPa. The intercept is about 4.80×10^6 A with an uncertainty of 0.83×10^6 A. The coefficient of determination is 0.64, which shows a statistically significant positive trend between the approximate total current of the dayside magnetopause and the solar wind pressure during southward IMF. Most magnetopause crossings events were observed during periods of lower solar wind dynamic pressure and higher magnetosonic mach numbers. The majority of southward magnetopause crossing events occur during moderate to high magnetosonic mach number, which typically causes the J × B force on the solar wind to occur at the magnetopause.
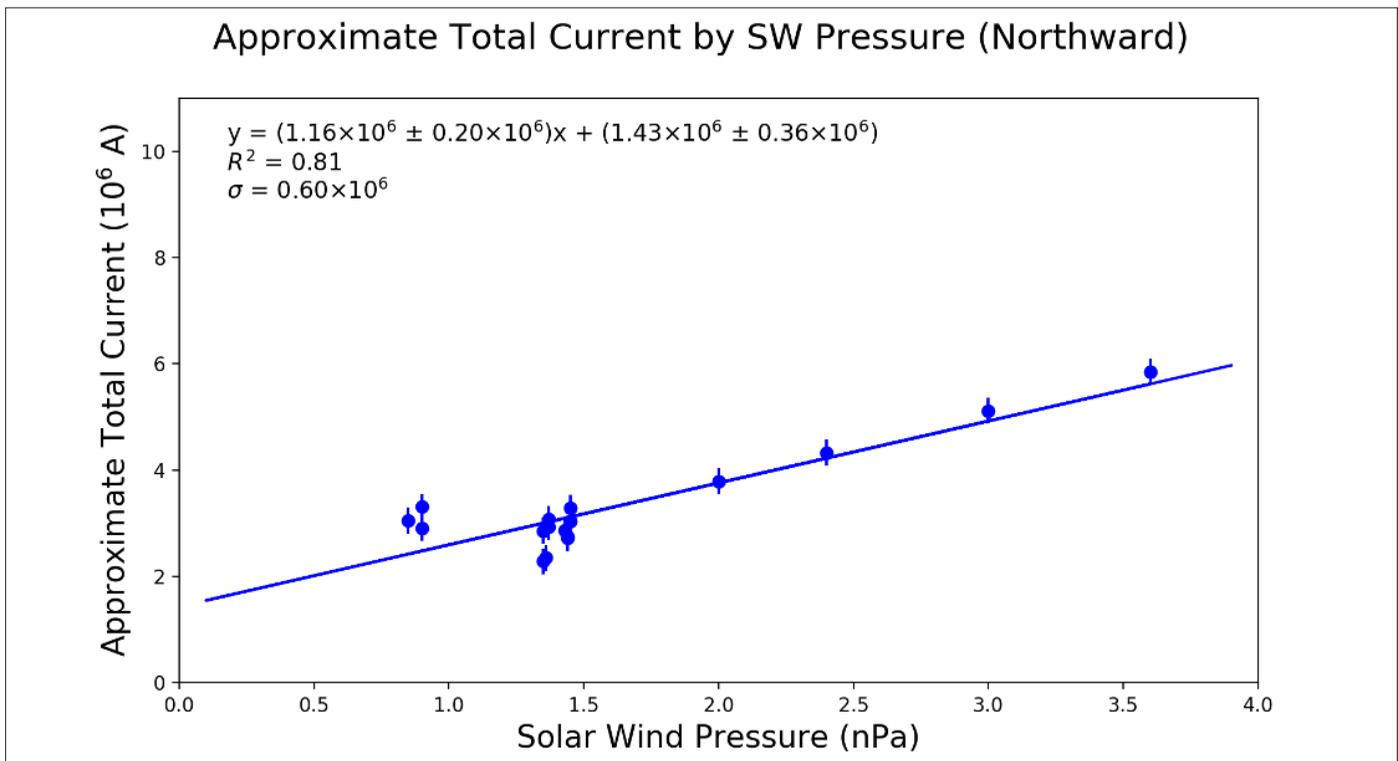
Figure 6. Scatterplot of approximate total current calculated from northward crossings compared to solar wind dynamic pressure at incident of magnetopause crossing events. Figure generated on 2020 June 14 using Python MatPlotLib.

Figure 6 reveals a comparable positive trend between approximate total current of the dayside magnetopause and solar wind pressure for about twenty northward magnetopause crossings. The trend is a rate of increase of 1.16×10^6 A/nPa during periods of northward IMF with an uncertainty of 0.20×10^6 A/nPa. The rate is slightly slower than the southward magnetopause crossing but not by a considerable value due to uncertainties calculated through standard deviations of slopes and intercepts. The intercept of the northward crossing events is much lower than the southward crossing events, which is reasonable since the change in magnetic field from southward IMF to northward magnetospheric field is much greater than the change between northward IMF to Earth's dipole field. The coefficient of determination is about 0.81, which confirms a statistically significant trend between approximate total current of the dayside magnetopause and solar wind dynamic pressure during northward IMF. Most of the northward magnetopause crossings were observed during instances of lower solar wind dynamic pressure and high magnetosonic mach numbers, similarly to the southward crossing events.

Discussions & Conclusions

Using a total of nearly eighty magnetopause crossings differentiated based on the z-component of the IMF, OMNIWeb and THEMIS data revealed a positive trend between total current and solar wind dynamic pressure during northward and southward IMF. The least-squares fit of the southward and northward crossing events result in coefficients of determinations of 0.64 and 0.81 each, which indicates statistical significance. A positive trend in both northward and southward IMF implies a direct relationship between solar wind dynamic pressure and approximate total current of the dayside magnetopause regardless of orientation of the IMF. The slopes of both the southward and northward events are nearly equivalent, which suggests the orientation of IMF is independent of the effect of solar wind dynamic pressure on the approximate total current of the dayside magnetopause. The balance between solar wind dynamic pressure and the magnetic pressure of the dipole field defines the shape and location of the magnetopause. Solar wind dynamic pressure compresses the dipole field, which corresponds to an increase in the electric current along the magnetopause. The intercept of the magnetopause crossing events during southward IMF is much greater than the intercept of the magnetopause crossing events during northward IMF. This disparity is expected as change in magnetic field during northward IMF only occurs between closed field lines, while change in magnetic field during southward IMF occurs on both open and closed field and increases the total electric current.

This study models the approximate total current of the dayside magnetopause based on the current distribution at the nose; however, this is an ideal situation in which the shape of the dayside magnetopause is even and uniform. The calculations rely on the assumption that the magnetopause cavity is semi-circular. At the nose of the magnetopause, magnetic pressure is dominant in maintaining the force balance between solar wind and the magnetosphere. Toward the cusp, pressure balance is maintained dominantly by thermal pressure instead of magnetic pressure, so the shape of the magnetopause may not be as elliptical as assumed in the calculations (Shue and Chao 2013). This may account for slight differences between the northward and southward events, as northward events do not cause erosion of the dayside magnetopause. Minimal asymmetries did not appear to cause major discrepancies between the northward and southward events.

Further analysis could be done by accumulating more magnetopause crossing events to be analyzed. Most of the magnetopause crossing events were accumulated during periods of low solar wind pressure, and larger solar wind pressure could slightly affect the trendlines. Larger solar wind pressure may skew upward, as larger solar wind pressure may compress the magnetic field further. An even dispersion of data is necessary to determine if this phenomenon occurs on a broad scale of magnetopause crossings. Also, more events with lower magnetosonic mach number could be accumulated to have an even variety of northward and southward magnetopause crossing events. THEMIS data is limited by availability and clarity, and future studies could include observations made by other satellite missions.

Acknowledgements

References

Bevington, P. R., Robinson, D. K. 2003. Data reduction and error analysis for the physical sciences. 3rd ed. New York (NY): McGraw-Hill Higher Education.

Bonde, R. E. F., Lopez, R. E., Wang, J. Y. 2018. The effect of IMF fluctuations on the subsolar magnetopause position: a study using a global MHD model. J Geophys Res: Space Phys. 123(4):2598–2604.

Kivelson, M. G., Russell, C. T. 1995. Introduction to space physics. 1st ed. Cambridge (UK): Cambridge University Press.

Lopez, R. E., Gonzalez, W. D. 2017. Magnetospheric balance of solar wind dynamic pressure. Geophys Res Lett. 44(7):2991–2999.

Schwenn, R. 2006. Space weather: the solar perspective. Living Rev Solar Phys. 3:2.

Shue, J. H., Chao, J. K. 2013. The role of enhanced thermal pressure in the earthward motion of the Earth's magnetopause. J Geophys Res: Space Phys. 118:3017–3026.

Sibeck, D. G., Lopez, R. E., Roelof, E. C. 1991. Solar wind control of the magnetopause role in determining the magnetopause shape, location, and motion. J Geophys Res. 96(A4):5489–5495.

Siscoe, G. 2000. The space-weather enterprise: past, present, and future. J Atmospheric Sol-Terr Phys. 62(14):1223–1232.

Southwood, J., Kivelson, G. 1990. The magnetohydrodynamic response of the magnetospheric cavity to changes in solar wind pressure. J Geophys Res: Space Phys. 95(A3):2301–2309.

Zweibel, E. G., Yamada, M. 2016. Perspectives on magnetic reconnection. Proc Royal Soc A. 472(2196):20160479.

OPSINS IN THE SKIN OF TWO COLOR FORMS OF COMMON LESSER EARLESS LIZARDS (*HOLBROOKIA MACULATA*)

Chris McDaniels

Biology Major

Faculty Mentor: Matthew Fujita, Ph.D.

Department of Biology

ABSTRACT

Opsins are transmembrane proteins that interact with light and play a role in vision formation in the eye. In extraocular locations, opsins take on different non-visual roles, many of which are not well understood. I investigated opsins in the skin of two color forms (pale and dark) of Common Lesser Earless Lizards (*Holbrookia maculata*). Transcriptomes from the skin were sequenced and assembled and then made into nucleotide databases. I used BLAST+ to search for genes in the transcriptome databases that are similar to opsin genes in other squamates. I then aligned amino acid sequences of genes from the blast searches and inferred phylogenetic trees. Orthologs from at least one color form of *H. maculata* were found for the opsins LWS, OPN3, OPN5, RGR, RH1, RRH, and SWS2. Paralogs were found for OPN5 and possibly RH1 and SWS2. Comparisons of opsins between the two color forms show highly conserved sequences with little divergence. More work needs to be done to (1) confirm the identities, structures, and functions of these extraocular opsins, especially OPN5, (2) how the structure and function of the opsins differ between the two forms, and (3) how the opsins influence the behavior and ecology of these lizards.

Introduction

Organisms have developed numerous systems to sense their environment and react to biotic and abiotic stimuli. These systems include the five basic senses of vision, hearing, touch, taste, and smell but also other sensory modalities such as electroreception, magnetoception, and echolocation (Dangles et al., 2009). Vision in particular is an important sense that is sensitive enough to respond to even a single photon of light (Hecht et al., 1942). The perception of light dictates many vital behaviors such as foraging, predator-prey interactions, locomotion, social communication, and sexual reproduction (Martin, 2012). My research focuses on characterizing the molecules that permit lizards to detect light.

Opsins are transmembrane proteins that are involved in the photoreception processes of vertebrate and invertebrate animals. Opsins consist of seven α-helices bound to a chromophore and make up photopigments found in photoreceptor cells. Traditionally, opsins were believed to be limited to the eye and only play a role in vision formation (Leung and Montell, 2017). These visual opsins are rhodopsin (RH1) in rods and the cone opsins (SWS1, SWS2, LWS, and RH2). They function in the retina when a chromophore absorbs light and undergoes photoisomerization. This causes a conformation change in the opsin that activates G-protein phototransduction cascades, which sends a signal to the brain (Terakita, 2005).

Contrary to classical beliefs, opsins do not function only in vision formation and are not exclusive to the eye. In 1994, research involving the pineal gland of chickens, an endocrine gland responsible for regulating circadian rhythm, revealed the presence of the first known nonvisual opsin: pinopsin (Okano et al., 1994). In the following decades, many more nonvisual opsins were identified along with insight into their functions. Nonvisual opsins are present in most animals and have been found in extraocular locations such as pineal organs and skin. It has also been discovered that the traditional visual opsins, such as rhodopsin, are present in extraocular locations and perform nonvisual functions. The nonvisual roles of these opsins include pupil dilation, entrainment of circadian rhythms, melatonin release, thermosensation, and relaxation of blood vessels (Leung and Montell, 2017).

Reptiles in particular are ideal candidates for investigating the presence of extraocular opsins and their nonvisual roles. As poikilotherms, reptiles rely on external environmental factors, a major factor being light, to thermoregulate. This significant reliance on light suggests a strong presence of photoreceptive extraocular opsins, and some have already been identified. Pinopsin (P-opsin) has been detected in the pineal gland of Green Anoles (*Anolis carolinensis*) and other lizards and is responsible for melatonin synthesis and regulation of the circadian rhythm (Bertolucci and Foà, 2004). Skin is another area with the potential to express opsins; in this case, the opsins can detect the color characteristics of their environment and allow the animal to respond by altering its skin patterns, enhancing camouflage. In the melanophores of Moorish Geckos (*Tarentola mauritanica*), the short wavelength-sensitive opsin (SWS1) was expressed. The SWS1 opsin, known for its vision formation role in the eye, was found to have a nonvisual role. Experiments revealed that the SWS1 opsin in the skin of the thorax, rather than in the eyes, is responsible for the ability of these geckos to detect light and darken or lighten their coloration to match the surrounding environment (Fulgione et al., 2014). How these opsins in the skin interact with light is important because light detection and coloration in reptiles affects vital behaviors such as thermoregulation, circadian rhythms, camouflage, social communication, and reproduction (Kelley and Davies, 2016). Lizards in the family Phrynosomatidae are good choices for studying extraocular opsins since they are diurnal lizards that are native to arid and light-intense environments. A study examined the parietal eye of one species of phrynosomatid, Common Side-Blotched Lizards (*Uta stansburiana*), since photoreceptors in the parietal eye showed chromatic antagonism, polarizing responses to different wavelengths of light, which is not known in any other photoreceptor. Examination of the cDNA library of the parietal eye revealed a previously unknown opsin, now known as

parietopsin (Su et al., 2006). My study analyzes the transcriptomes from the skin of two different color forms of Common Lesser Earless Lizards (*Holbrookia maculata*), to address two research questions:

(1) What are the opsins that are expressed in the skin?
(2) Are there any differences between opsins from the two different color forms of *H. maculata*?

Materials and Methods

Specimens

This study uses two specimens of *H. maculata*: one color form, "pale," was collected in a region of white gypsum sand near Holloman Air Force Base in New Mexico (MKF963). The other color form, "dark," a more typical form of this species, was collected in a region of darker soil from Comanche National Grassland in Colorado (MKF964). These animals were collected using proper collecting permits and under UTA IACUC protocol #A16.010. Dorsal skin samples from each lizard were collected and stored in RNALater (Qiagen), and the specimens have been deposited in the Amphibian and Reptile Diversity Research Collection.

Transcriptome Sequencing and Assembly

Total RNA was extracted from the two skin samples using the Promega Total SV RNA Extraction kit (Promega). The quality of the RNA was assessed using a Bioanalyzer, which compares the relative peaks of two target rRNA molecules to determine whether the sample is adequate for library preparation. Because this value, called the RNA Integrity Number (RIN), was > 7 for both samples, they were approved for sequencing at the North Texas Genome Center (NTGC). The NTGC prepared the library and subsequently sequenced the samples on a NovaSeq6000.

The data were processed to remove low quality reads using Trimmomatic v.32 and the following parameters to trim and remove failed reads: a 4-base sliding window trimming nucleotides with a Q score <5 and discarding reads <25bp long (Bolger et al., 2014; MacManes, 2014). To ensure quality trimming and filtering, the processed reads were run through FASTQC v0.10.1 (Babraham Bioinformatics) to evaluate read quality, length, and the number of reads retained. *De novo* assemblies were carried out using Trinity short-read assembler v2.2.1 for each sample (Grabherr et al., 2011). TransDecoder v3.0.1 was used to identify candidate coding genes from our assembled transcript sets with the longest open reading frames (ORFs) (Haas and Papanicolaou, 2015). To maximize the number of ORFs captured and to ensure we did not lose any potential coding genes, TransDecoder's optional homology search was run against the PFAM database (Finn et al., 2016).

Data Analysis

Using the program BLAST+ (2.10.1), I created a transcriptome database for each color form of *H. maculata* (Camacho et al., 2009). I searched the online database GenBank for protein coding regions of opsins in closely related squamates (Sayers et al., 2020). I selected nonvisual opsins that are known in vertebrates: neuropsin (OPN5), melanopsin (OPN4), encephalopsin/panopsin (OPN3), parietopsin, parapinopsin, pinopsin, retinal G protein-coupled receptor (RGR), retinal pigment epithelium-derived rhodopsin homolog/peropsin (RRH), teleost multiple tissue opsin (TMT), and vertebrate ancient opsin (VA). Because it was discovered that a visual opsin played a role in the skin of geckos, I also included visual opsins in my search: long-wave sensitive opsin (LWS), short-wave sensitive opsin 1 (SWS1), short-wave sensitive opsin 2 (SWS2), rhodopsin

1 (RH1), and rhodopsin 2 (RH2). The protein coding regions (query sequences) of these opsins were then used in tblastx searches with the *H. maculata* transcriptome databases (e-value cutoff of 1e-10). The program tblastx translates the database and query nucleotide sequences into their six different reading frames (three forward and three backward) and then conducts six different searches against the database based on amino acid sequences. Based on this initial blast search, I identified 92 genes from the *H. maculata* transcriptomes that matched at least one of the opsins that I collected from GenBank. This initial collection of genes was then used to establish an "opsin-only" database for *H. maculata*. Using this third database, I performed an additional tblastx search using a more stringent e-value cutoff (1e-50).

Using the program MACSE (2.03), I aligned the genes between the *H. maculata* specimens and those from the other squamates (Ranwez et al., 2011; Ranwez et al., 2018). MACSE aligns the nucleotide sequences by comparing their respective amino acid translations. I imported the resulting alignments into the program Geneious Prime 2020.1.2 (Biomatters), which allowed me to compare the aligned genes using phylogenetic trees and distances. Genes that were too divergent or too small to be full genes were removed from the alignments. Final phylogenetic trees were made with the *H. maculata* genes that are homologous to the other squamate opsin genes.

Results

Transcriptome Assembly

After the assembly using Trinity and filtering using Transdecoder, there were 46,558 transcripts for the pale *H. maculata* and 54,268 for the dark *H. maculata*. These numbers are likely larger than the number of genes in the genome and thus represent isoforms, alternative transcripts, or perhaps sequencing errors resulting in mis-assembled sequences.

GenBank Searches

A total of 44 genes were found after searching for 15 different opsins (Table 1). Genes were found for each opsin except TMT; however, TMT opsin did show up as a conserved domain in a "pinopsin-like" gene (XM_020811580.1) and a "parapinopsin-like" gene (XM_020784021.1). Coding sequences of the opsin genes were taken from Common Side-Blotched Lizards (*Uta stansburiana*), Green Anoles (*Anolis carolinensis*), and Central Bearded Dragons (*Pogona vitticeps*). One coding sequence from Western Terrestrial Garter Snakes (*Thamnophis elegans*) was used when another species could not be used as an outgroup.

Blast Searches

In the initial blast searches with the first databases (e-value cutoff of 1e-10), a total of 92 *H. maculata* genes blasted to the query sequences. Thirty-nine of the genes were from the pale specimen, and 53 genes were from the dark specimen. In the blast search with the refined "opsin-only" database (e-value cutoff of 1e-50), a total of 38 *H. maculata* genes blasted to the query sequences (Table 2). Twenty-one of the genes were from the pale specimen, and 17 genes were from the dark specimen. All 44 of the query sequences had matches with *H. maculata* genes from the initial database (e-value cutoff of 1e-10). With the refined database, only 36 of the query sequences had matches (e-value cutoff of 1e-50). All 14 opsin groups had results in the initial blast searches. In the refined blast search, melanopsin (OPN4) was the only opsin group that did not have any results.

Alignments and Phylogenetic Trees

Holbrookia maculata genes were identified as homologous for seven different opsins, and phylogenetic trees were made for each opsin: LWS, OPN3, OPN5, RGR, RH1, RRH, and SWS2. No genes were identified as homologous to parapinopsin, parietopsin, pinopsin, RH2, SWS1, or VA opsin; all genes that matched with these opsins from the blast searches matched other opsins more closely. A tree was also made comparing the opsin genes from *U. stansburiana*.

Long-Wave Sensitive Opsin (LWS)

Eleven *H. maculata* genes (7 pale, 4 dark) blasted to LWS; ten of the genes are excluded from the final tree because they are either too divergent or show higher homology with a different opsin. LWS genes in *T. elegans* (XM_032212316.1) and *U. stansburiana* (DQ129869.1) are included in the tree with *T. elegans* as the outgroup (Fig. 1). No gene from the dark specimen is homologous to LWS opsin. The single gene from the pale specimen (Gene 78345) is orthologous with the LWS genes from *T. elegans* and *U. stansburiana* and displays an amino acid identity of 88.4% to *T. elegans* and 86.4% to *U. stansburiana*. *Thamnophis elegans* and *U. stansburiana* display an 87.9% identity to each other.

Encephalopsin/Panopsin (OPN3)

Three *H. maculata* genes (1 pale, 2 dark) blasted to OPN3; one gene is excluded from the final tree for being too divergent. OPN3 genes in *P. vitticeps* (XM_020788365.1) and *A. carolinensis* (XM_008123887.2) are included in the tree with *P. vitticeps* as the outgroup (Fig. 1). One gene from the pale specimen (Gene 28867) and one from the dark specimen (Gene 18107) are homologous to each other and orthologous to the OPN3 genes in *P. vitticeps* and *A. carolinensis*. The two *H. maculata* genes display an amino acid identity of 100% to each other, 78.1–91.3% to *A. carolinensis*, and 76.0–89.9% to *P. vitticeps*. *Pogona vitticeps* and *A. carolinensis* display an identity of 73.4% to each other.

Neuropsin (OPN5)

Ten H. maculata genes (7 pale, 3 dark) blasted to OPN5; six of them are excluded from the final tree for being too divergent. Two OPN5 genes in *P. vitticeps* and two in *A. carolinensis* are included in the tree (Fig. 1); three *P. vitticeps* genes (XM_020779553.1, XM_020790964.1, and XM_020802814.1) and two *A. carolinensis* genes (XM_003220651.3 and XM_003223528.3) are removed for being too divergent. The tree shows two distinct groups of OPN5 genes. Group A consists of one gene from the pale specimen (Gene 34036) and one from the dark specimen (Gene 78000), one gene from *P. vitticeps* (XM_020801528.1), and one gene from *A. carolinensis* (XM_003215369.3). In group A, the two *H. maculata* genes display an amino acid identity of 100% to each other, 83.0–84.6% to *A. carolinensis*, and 84.7–88.2% to *P. vitticeps*. *Pogona vitticeps* and *A. carolinensis* display an identity of 76.5% to each other. The tree shows the *P. vitticeps* gene to be closer to the *H. maculata* genes than the *A. carolinensis* gene is. Group B consists of one gene from the pale specimen (Gene 15298) and one from the dark specimen (Gene 27413), one gene from *P. vitticeps* (XM_020796739.1), and one gene from *A. carolinensis* (XM_008116579.2). In group B, the two *H. maculata* genes display an identity of 99.7% to each other, 87.7–88.0% to *A. carolinensis*, and 74.4–74.6% to *P. vitticeps*. *Pogona vitticeps* and *A. carolinensis* display an identity of 72.3% to each other. The tree shows the *A. carolinensis* gene is closer than the *P. vitticeps* gene to the *H. maculata* genes. The amino acid identities between the *H. maculata* genes from the different groups are 33.9% between the two pale genes, 32.6% between the two dark genes, and 32.6–33.9% between the pale and dark genes.

Retinal G Protein-Coupled Receptor (*RGR*)

Three *H. maculata* genes (2 pale, 1 dark) blasted to RGR; one of them is excluded from the final tree because it is too divergent. RGR genes in *P. vitticeps* (XM_020796842.1) and *A. carolinensis* (XM_003223263.3) are included in the tree with *P. vitticeps* as the outgroup (Fig. 1). One gene from the pale specimen (Gene 34274) and one from the dark specimen (Gene 16473) are homologous to each other and orthologous to the RGR genes in *P. vitticeps* and *A. carolinensis*. The two *H. maculata* genes display an amino acid identity of 99.2% to each other, 93.7–95.1% to *A. carolinensis*, and 88.7–89.6% to *P. vitticeps*. *Pogona vitticeps* and *A. carolinensis* display an identity of 86.2% to each other.

Rhodopsin 1 (*RH1*)

Fourteen *H. maculata* genes (6 pale, 8 dark) blasted to RH1; six genes are excluded from the final tree because they are either too short or show higher homology with a different opsin. An RH1 gene in *U. stansburiana* (DQ100323.1) is included in the tree (Fig. 2). Only one *H. maculata* gene (dark) is orthologous to the RH1 gene in *U. stansburiana*; however, seven other *H. maculata* genes (4 pale, 4 dark) are included in the tree since RH1 is the opsin they match most closely. The tree can be split into groups A, B, C, and D, with group D as the outgroup. Group A consists of *U. stansburiana* and the orthologous *H. maculata* gene (dark). This orthologous gene (Gene 46621) displays an amino acid identity of 98.9% to *U. stansburiana*. Group B, the sister to group A, consists of one gene from the pale specimen (Gene 61425) and one from the dark specimen (Gene 39560), and the two genes display an identity of 94.9% to each other. Group B displays a 79.1–79.6% identity to the *H. maculata* gene and 79.9–81.4% to *U. stansburiana* in group A. Group C is the next closest to groups A and B and consists of one gene from the pale specimen (Gene 46019) and one from the dark specimen (Gene 59527); the two genes display an identity of 100% to each other. Group C displays a 80.9–81.2% identity to the *H. maculata* gene and 83.3–84.0% to *U. stansburiana* in group A. Group D, the most distant from group A, consists of three genes: one gene from the pale specimen (Gene 52702) and one from the dark specimen (Gene 39576) are homologous to each other. The third gene is from the pale specimen (Gene 52705). The two homologous genes display an identity of 99.2% to each other and an identity of 96.6–97.5% to the third gene. Group D displays an 82.2% identity to the *H. maculata* gene and 83.1–83.9% to *U. stansburiana* in group A.

Retinal Pigment Epithelium-Derived Rhodopsin Homolog/Peropsin (*RRH*)

Two *H. maculata* genes (2 dark) blasted to RRH; one of the genes is removed from the final tree for being too short. No genes from the pale specimen were found. One RRH gene in *P. vitticeps* (XM_020808834.1) and one in *A. carolinensis* (XM_008125246.2) are included in the tree with *P. vitticeps* as the outgroup (Fig. 2); one *A. carolinensis* gene (XM_008112114.2) is removed for being an almost identical copy of the other *A. carolinensis* gene. The *H. maculata* gene (Gene 90263) displays an amino acid identity of 94.3% to *A. carolinensis* and 90.8% to *P. vitticeps*. *Pogona vitticeps* and *A. carolinensis* display an identity of 92.2% to each other.

Short-Wave Sensitive Opsin 2 (*SWS2*)

Sixteen *H. maculata* genes (9 pale, 7 dark) blasted to SWS2; ten genes are excluded from the final tree because they are either too short, too divergent, or show higher homology with a different opsin. One SWS2 gene in *U. stansburiana* (DQ100326.1) and one in *A. carolinensis* (AF133907.1) are included in the tree (Fig. 2). No *H. maculata* genes are orthologous to the SWS2 genes in *U. stansburiana* and *A. carolinensis*; however, six *H. maculata* genes (4 pale, 2 dark) are included in the tree since SWS2 is the opsin they match most closely. The tree can be split into sister groups A, B, and C. Group A consists of the *U. stansburiana* and *A. carolinensis* genes; they display an amino acid identity of 92.3% to each other. Group B consists of one gene from the pale specimen (Gene 54488) and one from the dark specimen (Gene 88775), and the two genes display an identity of 100%

to each other. Group B displays an 84.7–85.2% identity to *U. stansburiana* and 83.8–84.67% to *A. carolinensis* in group A. Group C consists of three genes from the pale specimen and one from the dark specimen. One of the genes from the pale specimen (Gene 25255) and the gene from the dark specimen (Gene 19267) are homologous with an identity of 100% to each other. The other two genes from the pale specimen (Gene 25256 – the closest to the homologous genes; Gene 55302 – the furthest from the homologous genes within Group C) display an identity of 89.9–97.5% to the aforementioned homologous genes. Group C displayed an identity of 75.3–76.6% to *U. stansburiana* and 73.4–75.8% to *A. carolinensis* in group A.

Uta stansburiana Opsins

Seven opsin genes from *U. stansburiana* were aligned and made into a tree: parietopsin, pinopsin, LWS, SWS1, SWS2, RH1, and RH2. Parietopsin was used as the outgroup (Fig. 2). RH2 and RH1 are homologous, with the next closest relative being SWS2. SWS1 opsin is the next closest relative after SWS2, then LWS, pinopsin, and finally parietopsin.

Discussion

Opsins

Long-Wave Sensitive Opsin (*LWS*)

The only gene found is from the pale specimen of *H. maculata*. Most of the opsins match with genes from both the pale and dark specimens that show close homology; it is, therefore, unusual that a gene from the dark specimen was not found for LWS. The most likely explanation is that the LWS gene may not have been expressed in great quantities and was overlooked when sequencing the transcriptome. Other than the missing gene, the relationships reflected in the phylogenetic tree are expected, with *H. maculata* being most closely related to *U. stansburiana* and more distant to *T. elegans*. Because only one LWS gene was found and its closest relative is the gene from *U. stansburiana*, I am confident that the *H. maculata* sequence is an LWS ortholog. Typically, LWS is found in the eye as a cone opsin and has a peak sensitivity to light wavelengths of 500–570 nm (Katti et al., 2019). This LWS ortholog in the skin of *H. maculata* likely detects similar wavelengths, but the function of this opsin in an extraocular setting is unclear.

Encephalopsin/Panopsin (*OPN3*)

A gene was found for each of the color forms of *H. maculata*, and they have identical amino acid sequences. The relationships reflected in the phylogenetic tree are expected with the two *H. maculata* genes most closely related to *A. carolinensis* and more distant to *P. vitticeps*. Based on these relationships, I am confident that the *H. maculata* sequences are OPN3 orthologs. The function of OPN3 in squamates is unknown; in the skin of humans, it is said to regulate the production of melanin, but its dependence on light is debated (Ozdeslik et al., 2019; Regazzetti et al., 2018). These OPN3 orthologs in *H. maculata* might function in melanogenesis, but there is not enough evidence to draw any conclusions.

Neuropsin (*OPN5*)

Two groups of genes were found for OPN5 with each group containing one gene from each form of *H. maculata*. The *H. maculata* genes in group A have identical amino acid sequences. The relationships reflected in this portion of the phylogenetic tree are unexpected; the *H. maculata* genes are closer to the *P. vitticeps* gene than the *A. carolinesis* gene, despite *A. carolinensis* being a more closely related species. Such incongruence is a known problem in phylogenetics and may be due to limitations of the analysis or biological

factors (Rokas et al., 2003). Based on these relationships, I am confident that the *H. maculata* sequences are OPN5 orthologs. In Group B, the *H. maculata* genes have a 99.7% identity to each other. The relationships reflected in the phylogenetic tree are expected for Group B with *A. carolinensis* being the closest relative and *P. vitticeps* more distant. Based on these relationships, I am confident that the *H. maculata* sequences are also OPN5 orthologs. When *H. maculata* genes from the two groups are compared, they show extreme divergence with an identity of 32.6–33.9%. This might indicate that these two groups of OPN5 genes are paralogs. It is difficult to predict the function of these OPN5 opsins in *H. maculata*. In the deep brain of birds, it is proposed that OPN5 may regulate seasonal reproduction (Nakane et al., 2010). In the skin on the tails of sea snakes (*Aipysurus laevis*), OPN5 might contribute to tail phototaxis, an anti-predatory behavior that has not been found in other reptiles; OPN5 is not expressed in the tails of other snakes (Crowe-Riddell et al., 2019; Hauzman et al., 2019). Since the behavior in sea snakes is unique in reptiles and OPN5 is not found in the tails of other snakes, the OPN5 orthologs in *H. maculata* likely do not function that way. Perhaps OPN5 regulates seasonal behaviors like it might in birds; for now, there is too little information to make any sort of conclusions.

Retinal G Protein-Coupled Receptor (*RGR*)

A gene was found for each of the color forms of *H. maculata*, and they have 99.2% identical amino acid sequences. The relationships reflected in the phylogenetic tree are expected with the two *H. maculata* genes most closely related to *A. carolinensis* and more distant to *P. vitticeps*. Based on these relationships, I am confident that the *H. maculata* sequences are RGR orthologs. In mammals, RGR acts as a photoisomerase by binding all-*trans* retinal and converting it to 11-*cis* retinal thus generating a chromophore for other opsins as a part of the visual cycle (Terakita, 2005). These RGR orthologs in *H. maculata* may function in a similar way.

Rhodopsin 1 (*RH1*)

The only gene found to be homologous with the gene for RH1 in *U. stansburiana* is from the dark specimen of *H. maculata*. Considering most of the opsins match with genes from both the pale and dark specimens that show close homology, it is unusual that a gene from the pale specimen was not found for RH1. The most likely explanation is that the RH1 gene may not have been expressed in great quantities and was overlooked when sequencing the transcriptome. Because only one RH1 gene was found and its closest relative is the gene from *U. stansburiana*, I am confident that the *H. maculata* sequence is an RH1 ortholog. The high amino acid identity of 98.9% to *U. stansburiana* reinforces this conclusion. I also include several other *H. maculata* genes in the RH1 phylogenetic tree; this is because they show most homology to RH1 compared to other opsins in this study. These other genes can be split into three main groups that have at least one gene from each specimen, and genes within these groups display high identities to each other. When compared with *U. stansburiana*, these groups display high identities ranging from 79.9–84.0%. Because of this, it is unclear if these other genes represent possible paralogs of RH1 or if they represent other opsin genes. In the eyes of squamates, RH1 detects wavelengths of light at a peak of 500 nm and is sensitive to low levels of light (Katti et al., 2019). If any of these genes in *H. maculata* are RH1, they likely sense wavelengths similar to RH1 in the eye. The function of RH1 in the skin of squamates is unknown, but it may play a role in melanin production in response to ultraviolet light (Wicks et al., 2011).

Retinal Pigment Epithelium-Derived Rhodopsin Homolog/Peropsin (*RRH*)

The only gene found is from the dark specimen of *H. maculata*. Considering most of the opsins match with genes from both the pale and dark specimens that show close homology, it is unusual that a gene from the pale specimen was not found for RRH. The most likely explanation is that the RRH gene may not have been expressed in great quantities and was overlooked when sequencing the transcriptome. Other than

the missing gene, the relationships reflected in the phylogenetic tree are expected with *H. maculata* most closely related to *A. carolinensis* and more distant to *P. vitticeps*. Because only one RRH gene was found and its closest relative is the gene from *A. carolinensis*, I am confident that the *H. maculata* sequence is an RRH ortholog. In mammals, RRH behaves similarly to RGR in that it acts as a photoisomerase by binding all-*trans* retinal and converting it to 11-*cis* retinal (Terakita, 2005). The RRH homolog in *H. maculata* may function in a similar manner.

Short-Wave Sensitive Opsin 2 (SWS2)

The relationships expressed in the phylogenetic tree show no *H. maculata* genes to be orthologous to SWS2 in *A. carolinensis* and *U. stansburiana*. However, I did include other *H. maculata* genes because they still show higher homology to SWS2 than to other opsins in this study. These other genes can be split into two main groups that have at least one gene from each specimen, and genes within these groups display high identities to each other. When compared with *U. stansburiana*, these groups display high amino acid identities ranging from 75.3–85.2%. Because of this, it is unclear if these genes represent possible paralogs of SWS2 or if they represent other opsin genes. Typically, SWS2 is found in the eye as a cone opsin and has a peak sensitivity to light wavelengths of 400–470 nm, but the role it may have in the skin is unclear (Katti et al., 2019).

Uta stansburiana Opsins

I created a phylogenetic tree using the opsins from *U. stansburiana* to investigate the relatedness of the opsins. The relationships shown in this tree are consistent with the relationships of those opsins in other squamates (Wada et al., 2012). These relationships likely explain why many of the same *H. maculata* genes match with several opsins.

Absent Opsins

Homologous genes from the *H. maculata* transcriptomes could not be found for several opsins. For melanopsin (OPN4), no genes were found using the more stringent blast search. In mammals, OPN4 in the retina helps regulate circadian rhythms, but the function of this opsin in reptiles is less known (Hauzman et al., 2019). OPN4 genes have been expressed in the skin on the tail of the sea snakes *Aipysurus laevis* and *A. tenuis* and, as mentioned with OPN5, likely contribute to tail phototaxis (Crowe-Riddell et al., 2019). When searched for in other snakes, OPN4 was absent in other elapids, vipers, and colubrid snakes (Hauzman et al., 2019). This could explain why OPN4 was not expressed in the skin of *H. maculata* since there is no known phototactic behavior in this species similar to the sea snakes. For the opsins parapinopsin, parietopsin, pinopsin, RH2, SWS1, and VA, all the genes they blasted to match other opsins more closely. SWS1, a cone opsin with peak sensitivity to light wavelengths of 355–445 nm, is expressed in the skin of Moorish Geckos (*Tarentola mauritanica*) and plays a role in detecting light levels to aide in coloration change (Fulgione et al., 2014; Katti et al., 2019). However, in Tawny Dragons (*Ctenophorus decresii*) SWS1 (as well as SWS2, RH2, and LWS) is not expressed in the skin (Yewers et al., 2015). Since there is no evidence that *H. maculata* and *C. decresii* change coloration under different light intensities, this may explain why no SWS1 genes were found in the transcriptomes. For the other absent opsins, it is difficult to know whether these absences are shared among other squamates since there is a lack of studies using skin transcriptomes. The absence of these opsin genes suggests several possibilities: the genes that code for these opsins may be present but were not expressed; the genes were expressed but at a minimal amount that was not detected when sequencing the transcriptomes; or *H. maculata* may have lost the genes completely. The third possibility is unlikely because the absent opsins are present in the genomes of related squamates from similar light-intense habitats.

Comparison of the Two Color Forms

Past research has shown that the dorsal coloration of the two forms of *H. maculata* is strongly heritable rather than a product of its environments (Rosenblum, 2005). Since opsins interact with light and can affect coloration, I expected to see some differences between the gene sequences of the two forms. In OPN3, group A of OPN5, group C of RH1, and groups B and C (excluding the paralog) of SWS2, the homologous genes of the two color forms display identical amino acid sequences. In group B of OPN5, RGR, and groups B and D (excluding the paralogs) of RH1, the homologous genes display an identity of 99.2–99.7%. This shows that the opsin genes between the two color forms are not very divergent and are highly conserved. A few opsins, LWS, the RH1 ortholog, and RRH, have results from only one color form.

Transcriptomes represent only those genes that are expressed in particular cells and tissues, thus not all genes will be available in these datasets. Genes that are only expressed at low amounts may be missed during these analyses, which could explain why I found genes in only one of the forms. I also ran into cases where multiple genes blasted to several transcripts in each form, and these could represent paralogs. Given that the number of transcripts for each form was quite large, it is also possible that the assembly was imperfect and some of the results need to be verified by additional sequencing or using alternative methods, such as PCR-amplification of the genes and subsequent Sanger sequencing.

Future Directions

Research involving opsins in the skin of squamates is sorely lacking with only a few published studies to reference. In relation to *H. maculata*, future research should include confirming the identities, structures, and functions of these extraocular opsins; investigating how differences in the genes between the two forms may affect the structure and function of these opsins; and how the functions of these opsins influence the behavior and ecology of these lizards.

Acknowledgments

Table 1.

GenBank search results showing the opsin group name, species, and accession number of each opsin gene

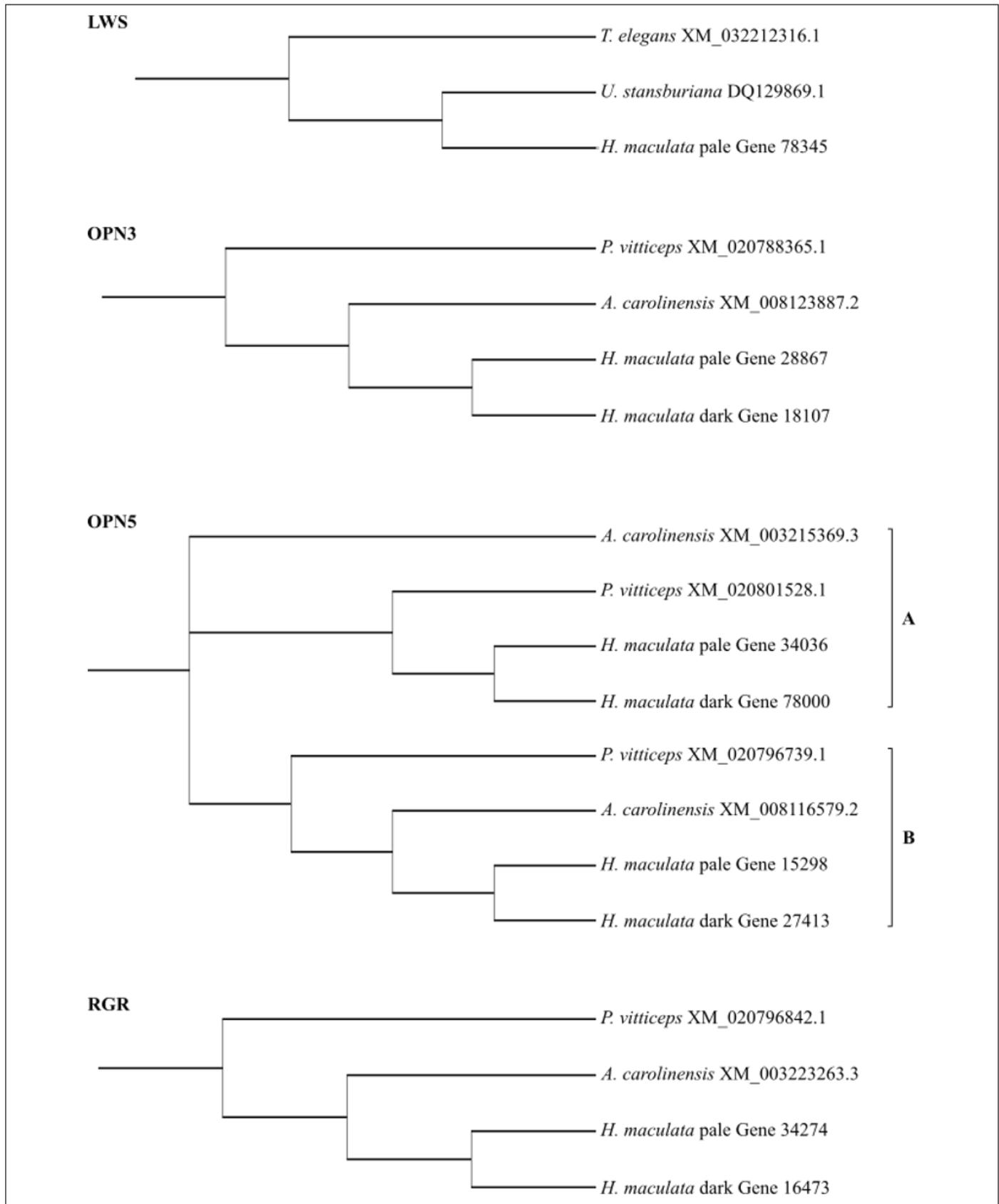|	*A. carolinensis*	*P. vitticeps*	*U. stansburiana*	*T. elegans*
LWS			DQ129869.1	XM_032212316.1
OPN3	XM_008123887.2	XM_020788365.1		
OPN4	XM_008119109.2 XM_008111055.1	XM_020805958.1 XM_020798651.1		
OPN5	XM_003223528.3 XM_008116579.2 XM_003220651.3 XM_003215935.2 XM_003215369.3	XM_020801528.1 XM_020790964.1 XM_020796739.1 XM_020802814.1 XM_020779553.1		
Parapinopsin	NM_001293131.1 XM_008107065.1	XM_020784021.1 XM_020804820.1		
Parietopsin			DQ100320.1	
Pinopsin	XM_016997727.1 XM_016999385.1	XM_020777959.1 XM_020811580.1	DQ100321.1	
RGR	XM_003223263.3	XM_020796842.1		
RH1			DQ100323.1	
RH2	NM_001291394.1		DQ100324.1	
RRH	XM_008112114.2 XM_008125246.2	XM_020808834.1		
SWS1	AH007736.2		DQ100325.1	
SWS2	AF133907.1		DQ100326.1	
VA	XM_008106312.2 NM_001293118.1 XM_003221042.3	XM_020795006.1		

Table 2.

Holbrookia maculata *genes from the pale and dark specimens that match to specific opsins from the tblastx results using the refined database (e-value cutoff of 1e-50). Bolded gene numbers are included in the phylogenetic trees for the corresponding opsins.*

	LWS	OPN3	OPN5	Parapinopsin	Parietopsin	Pinopsin
Pale	25255 25256 52702 52705 61425 **78345** 78346	**28867**	7783 7784 **15298** 32120 34030 34033 **34036**	25255 25256 28867 52702 52705 61425	25255 25256 52702 52705 61425	25255 25256 28867 52702 52705 61425
Dark	19267 39560 39576 88775	**18107** 87790	**27413** **78000** 78003	19267 39560 39576	19267 39576	19267 39560 39576 46621

|	RGR	RH1	RH2	RRH	SWS1	SWS2
Pale	**34274** 67298	25255 25256 **46019** **52702** **52705** **61425**	25255 25256 46019 52702 52705 55302 61425	None	25255 25256 52702 52705 54488 61425	8487 **25255** **25256** 46019 52702 52705 **54488** **55302** 61425
Dark	**16473**	19267 39558 39559 39560 **39576** **46621** **59527** 88775	19267 39558 39559 39560 39576 46621 59527 88775	44537 **90263**	19267 39560 39576 46621 88775	**19267** 39560 39576 46621 54766 59527 **88775**

Figure 1.

Phylogenetic trees for the opsins LWS, OPN3, OPN5, and RGR

Figure 2.

Phylogenetic trees for the opsins RH1, RRH, and SWS2, and U. stansburiana *opsins*
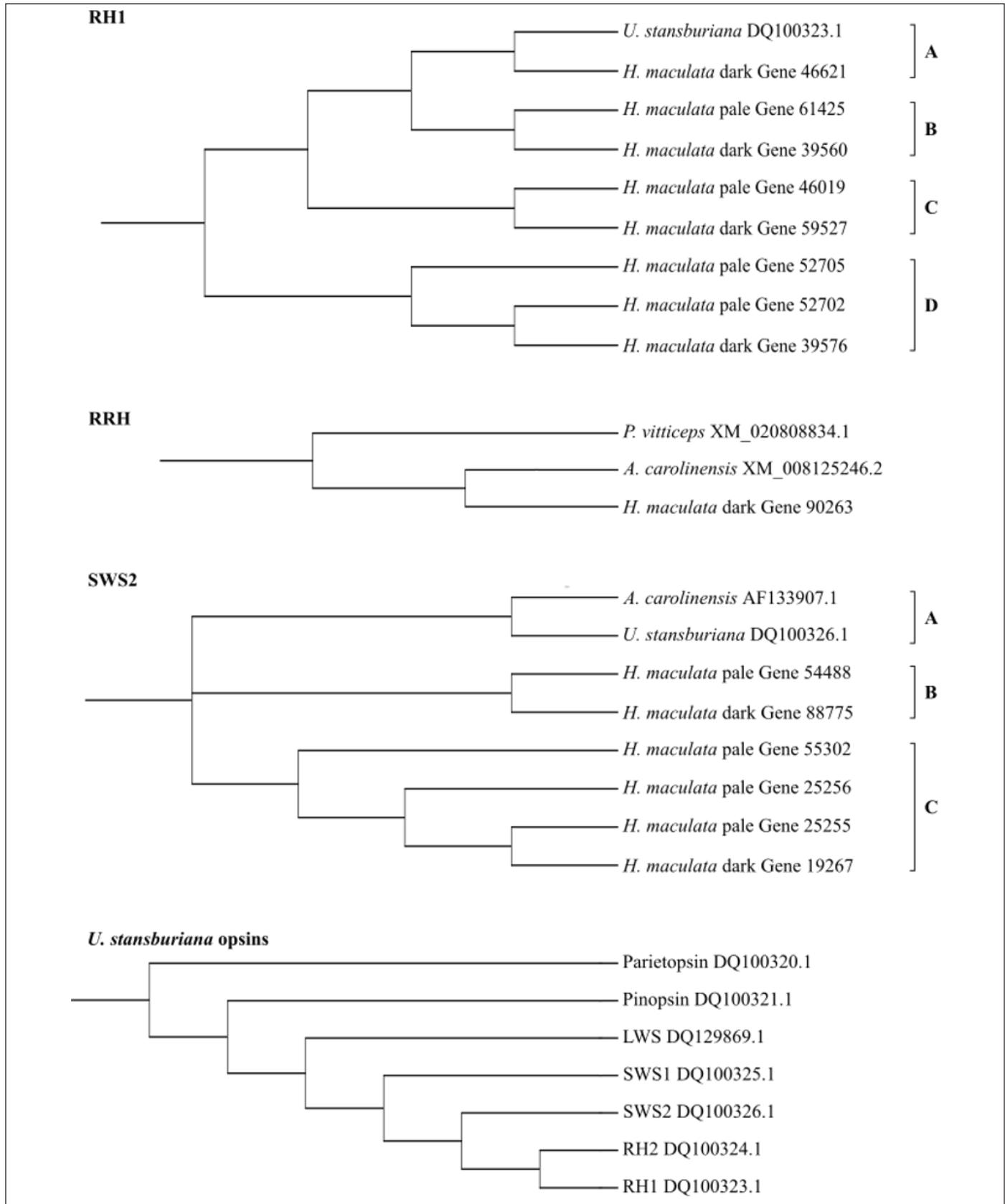
Literature Cited

Bertolucci, C., and A. Foà. 2004. Extraocular photoreception and circadian entrainment in nonmammalian vertebrates. Chronobiology International 21:501-519. https://doi.org/10.1081/cbi-120039813

Bolger, A. M., Lohse, M., and B. Usadel. 2014. Trimmomatic: a flexible trimmer for Illumina sequence data. Bioinformatics 30:2114-2120. https://doi.org/10.1093/bioinformatics/btu170

Camacho, C., Coulouris, G., Avagyan, V., Ma, N., Papadopoulos, J., Bealer, K., and T. L. Madden. 2009. BLAST+: architecture and applications. BMC Bioinformatics 10:421. https://doi.org/10.1186/1471-2105-10-421

Crowe-Riddell, J. M., Simões, B. F., Partridge, J. C., Hunt, D. M., Delean, S., Schwerdt, J. G., Breen, J., Ludington, A., Gower, D. J., and K. L. Sanders. 2019. Phototactic tails: evolution and molecular basis of a novel sensory trait in sea snakes. Molecular Ecology 28:2013-2028. https://doi.org/10.1111/mec.15022

Dangles, O., Irschick, D., Chittka, L., and J. Casas. 2009. Variability in sensory ecology: expanding the bridge between physiology and evolutionary biology. The Quarterly Review of Biology 84:51-74. https://doi.org/10.1086/596463

Finn, R. D., Coggill, P., Eberhardt, R. Y., Eddy, S. R., Mistry, J., Mitchell, A. L., Potter, S. C., Punta, M., Qureshi, M., Sangrador-Vegas, A., Salazar, G. A., Tate, J., and A. Bateman. 2016. The Pfam protein families database: towards a more sustainable future. Nucleic Acids Research 44:D279-D285. https://doi.org/10.1093/nar/gkv1344

Fulgione, D., Trapanese, M., Maselli, V., Rippa, D., Itri, F., Avallone, B., Van Damme, R., Monti, D. M., and P. Raia. 2014. Seeing through the skin: dermal light sensitivity provides cryptism in moorish gecko. Journal of Zoology 294:122-128. https://doi.org/10.1111/jzo.12159

Grabherr, M. G., Haas, B. J., Yassour, M., Levin, J. Z., Thompson, D. A., Amit, I., Adiconis, X., Fan, L., Raychowdhury, R., Zeng, Q., Chen, Z., Mauceli, E., Hacohen, N., Gnirke, A., Rhind, N., di Palma, F., Birren, B. W., Nusbaum, C., Lindblad-Toh, K., Friedman, N., and A. Regev. 2011. Full-length transcriptome assembly from RNA-Seq data without a reference genome. Nature Biotechnology 29:644-652. https://doi.org/10.1038/nbt.1883

Haas, B., and A. Papanicolaou. 2015. TransDecoder (find coding regions within transcripts). Available at https://githubcom/TransDecoder/TransDecoder. Accessed 17 May 2018.

Hauzman, E., Kalava, V., Bonci, D. M. O., and D. F. Ventura. 2019. Characterization of the melanopsin gene (Opn4x) of diurnal and nocturnal snakes. BMC Evolutionary Biology 19:174. https://doi.org/10.1186/s12862-019-1500-6

Hecht, S., Shlaer, S., and M. H. Pirenne. 1942. Energy, quanta, and vision. Journal of General Physiology 25:819-840. https://doi.org/10.1085/jgp.25.6.819

Katti, C., Stacey-Solis, M., Coronel-Rojas, N. A., and W. I. L. Davies. 2019. The diversity and adaptive evolution of visual photopigments in reptiles. Frontiers in Ecology and Evolution 7:352. https://doi.org/10.3389/fevo.2019.00352

Kelley, J. L., and W. I. L. Davies. 2016. The biological mechanisms and behavioral functions of opsin-based light detection by the skin. Frontiers in Ecology and Evolution 4:106. https://doi.org/10.3389/fevo.2016.00106

Leung, N. Y., and C. Montell. 2017. Unconventional roles of opsins. Annual Review of Cell and Developmental Biology 33:241-264. https://doi.org/10.1146/annurev-cellbio-100616-060432

MacManes, M. D. 2014. On the optimal trimming of high-throughput mRNA sequence data. Frontiers in Genetics 5:13. https://doi.org/10.3389/fgene.2014.00013

Martin, G. R. 2012. Through birds' eyes: insights into avian sensory ecology. Journal of Ornithology 153:23-48. https://doi.org/10.1007/s10336-011-0771-5

Nakane, Y., Ikegami, K., Ono, H., Yamamoto, N., Yoshida, S., Hirunagi, K., Ebihara, S., Kubo, Y., and T. Yoshimura. 2010. A mammalian neural tissue opsin (Opsin 5) is a deep brain photoreceptor in birds. Proceedings of the National Academy of Sciences of the United States of America 107:15264-15268. https://doi.org/10.1073/pnas.1006393107

Okano, T., Yoshizawa, T., and Y. Fukada. 1994. Pinopsin is a chicken pineal photoreceptive molecule. Nature 372:94-97. https://doi.org/10.1038/372094a0

Ozdeslik, R. N., Olinski, L. E., Trieu, M. M., Oprian, D. D., and E. Oancea. 2019. Human nonvisual opsin 3 regulates pigmentation of epidermal melanocytes through functional interaction with melanocortin 1 receptor. Proceedings of the National Academy of Sciences 116:11508-11517. https://doi.org/10.1073/pnas.1902825116

Ranwez, V., Douzery, E. J. P., Cambon, C., Chantret, N., and F. Delsuc. 2018. MACSE v2: toolkit for the alignment of coding sequences accounting for frameshifts and stop codons. Molecular Biology and Evolution 35:2582-2584. https://doi.org/10.1093/molbev/msy159

Ranwez, V., Harispe, S., Delsuc, F., and E. J. P. Douzery. 2011. MACSE: multiple alignment of coding sequences accounting for frameshifts and stop codons. PLOS ONE 6:e22594. https://doi.org/10.1371/journal.pone.0022594

Regazzetti, C., Sormani, L., Debayle, D., Bernerd, F., Tulic, M. K., De Donatis, G. M., Chignon-Sicard, B., Rocchi, S., and T. Passeron. 2018. Melanocytes sense blue light and regulate pigmentation through opsin-3. The Journal of Investigative Dermatology 138:171-178. https://doi.org/10.1016/j.jid.2017.07.833

Rokas, A., Williams, B. L., King, N., and S. B. Carroll. 2003. Genome-scale approaches to resolving incongruence in molecular phylogenies. Nature 425:798-804. https://doi.org/10.1038/nature02053

Rosenblum, E. B. 2005. The role of phenotypic plasticity in color variation of tularosa basin lizards. Copeia 2005:586-596. https://doi.org/10.1643/CP-04-154R1

Sayers, E. W., Cavanaugh, M., Clark, K., Ostell, J., Pruitt, K. D., and I. Karsch-Mizrachi. 2020. GenBank. Nucleic Acids Research 48:D84-D86. https://doi.org/10.1093/nar/gkz956

Su, C. Y., Luo, D. G., Terakita, A., Shichida, Y., Liao, H. W., Kazmi, M. A., Sakmar, T. P., and K. W. Yau. 2006. Parietal-eye phototransduction components and their potential evolutionary implications. Science 311:1617-1621. https://doi.org/10.1126/science.1123802

Terakita, A. 2005. The opsins. Genome Biology 6:213. https://doi.org/10.1186/gb-2005-6-3-213

Wada, S., Kawano-Yamashita, E., Koyanagi, M., and A. Terakita. 2012. Expression of UV-sensitive parapinopsin in the iguana parietal eyes and its implication in UV-sensitivity in vertebrate pineal-related organs. PLOS ONE 7:e39003. https://doi.org/10.1371/journal.pone.0039003

Wicks, N. L., Chan, J. W., Najera, J. A., Ciriello, J. M., and E. Oancea. 2011. UVA phototransduction drives early melanin synthesis in human melanocytes. Current Biology 21:1906-1911. https://doi.org/10.1016/j.cub.2011.09.047

Yewers, M. S., McLean, C. A., Moussalli, A., Stuart-Fox, D., Bennett, A. T., and B. Knott. 2015. Spectral sensitivity of cone photoreceptors and opsin expression in two colour-divergent lineages of the lizard *Ctenophorus decresii*. The Journal of Experimental Biology 218:1556–1563. https://doi.org/10.1242/jeb.119404

PROPERTIES OF TWO-ELECTRON TOPOLOGIES FOR NEUTRINOLESS DOUBLE BETA DECAY IN XENON GAS

Jacqueline Baeza-Rubio

Physics Major

Faculty Mentor: Benjamin Jones, Ph.D.

Physics Department

ABSTRACT

Since the neutrino was first postulated by Wolfgang Pauli, it has been a veritable front for new physics. The neutrino may be a Majorana fermion, meaning that it is its own antiparticle, a characteristic not shared by any other massive particle in the standard model. The discovery of Majorana fermions would have broad implications, most notably giving insight into the matter-antimatter imbalance in our universe. The best-known method for determining whether a neutrino is a Majorana fermion is to observe a hypothesized rare process known as neutrinoless double beta decay ($0\nu\beta\beta$). The Neutrino Experiment with a Xenon TPC (NEXT) searches for this decay by looking at the signal shape and energy of the electrons emitted during the decay of xenon-136. One of the largest obstacles in the development of this detector is its intrinsic sensitivity to the far more common counterpart of $0\nu\beta\beta$, two-neutrino double beta decay ($2\nu\beta\beta$), as well as other background sources in the same energy range. This study presents a computational analysis of the $2\nu\beta\beta$ events that represent one of the most important backgrounds to $0\nu\beta\beta$ in double beta decay experiments, such as NEXT. Through analysis of NEXT-White experiment data, we have been able to confirm low systematic uncertainties due to the double beta decay model. Specifically, the variance of the angle between the two outgoing electrons, or the electron opening angle.

1. Introduction

For the better part of a century, physicists have sought to find the "Majorana neutrino." This elusive particle is theorized to be its own antiparticle counterpart. Several experiments aim to prove the existence of such a particle by searching for a rare nuclear decay that is hypothesized to occur if and only if the neutrino, a neutrally charged particle, is a Majorana particle. The Neutrino Experiment with a Xenon Time Projection Chamber (NEXT) is one current investigation into this rare species of decay. Double beta decay has been observed in the nucleus of certain isotopes, such as xenon-136. In this decay, two neutrons in the nuclei decay into protons while simultaneously emitting two electrons and two antineutrinos, as seen in Fig. 1. If neutrinos are Majorana particles, physicists should be able to detect a similar process of neutrinoless double beta decay (0νββ) in which the two neutrinos or antineutrinos emitted, as in ^{136}Xe, annihilate each other.

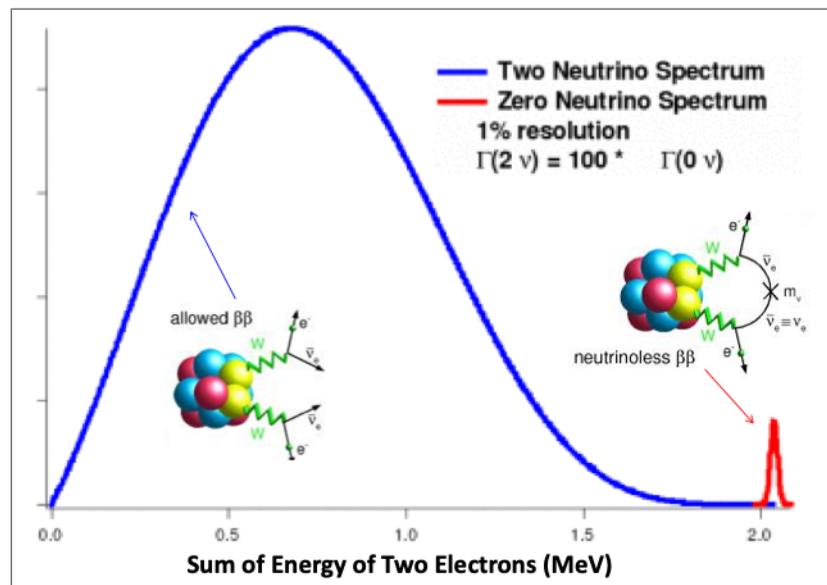Figure 1. The rate of each event (2νββ and 0νββ) as a function of the decay energy. The blue curve is the measured 2νββ spectrum, while the red curve is the calculated region where 0νββ should occur.

NEXT is a time projection chamber (TPC), a device that was built to observe 0νββ. The detector is filled with high-pressure (15 bar) xenon gas that emits two electrons[1] when decaying into barium. This process causes ionization, ejecting electrons that can be detected in the TPC[2] by light sensors that are located on the tracking plane made of silicon photo multipliers. This allows us to reconstruct the position and shape of the event. The ionization electrons naturally drift to the positively charged anode and through an electroluminescence (EL) region, where the electrons are accelerated and produce EL light in the gas. The EL region then produces more light to make signals more detectable.[3] The photons are then captured in an energy plane made of photo multiplier tubes, and their energy is later read out as data. With this data, the NEXT collaboration can reconstruct the path of the particles from the decay as well as determine the total energy of the event. This is important since the energy of 2νββ is different from the energy of 0νββ, as seen in Fig. 1. With a high enough sensitivity, the detector can distinguish between 2νββ and 0νββ.

This study presents a series of computational analyses that contribute to efforts in advancing the sensitivity of NEXT. This computational study focuses on the performance of the NEXT-White experiment. To extract small signals from radioactive background samples, the data is cut to exclude portions that are

filled with background events. These cuts include fiducial cuts calculated from the size of the detector and topological cuts that restrict signal event size and shape parameters of the forecasted 2νββ and 0νββ events. The shape of a 2νββ event is defined as a track with two electron "blobs" at each end (a blob being the energy deposited in a sphere around each track endpoint from the electron). It is important to note that background signals are distinct because they have only one electron blob and therefore allow for the selection of signal events through topological screening. With that said, simulated Monte Carlo 2νββ events have been analyzed to determine how robust the given cuts must be to account for the uncertainty caused by the nuclear structure.

2. Analysis and Methods

Monte Carlo (MC) simulations rely on the generation of random samples in order to obtain deterministic results to serve as a forecast model . Therefore, by using MC simulations modeled off NEXT-White data, five efficiency cuts were recreated to analyze two-electron events: an inclusive cut, a fiducial cut, a single-track cut, an overlapped blob energy cut, and a blob energy cut. These cuts cover general selection cuts and topological selection cuts in order to separate radioactive background events that could produce signal-like events (The general selections refer to events that occur in the fiducial volume, while the topological selections all refer to restrictions based on size and shape of the event).[2] With this analysis, the sensitivity towards modeled systematic uncertainties has been tested by determining how well the algorithm in place cuts radioactive background samples.
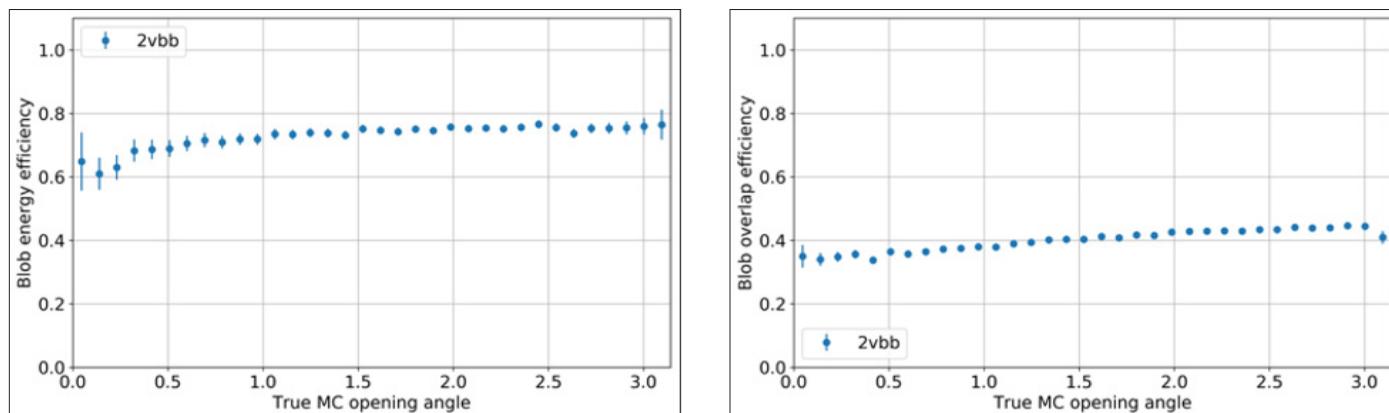
2.1 Efficiency Cuts

The inclusive cut distinguishes between two light signals that occur inside the TPC: signal 1 (S1) and signal 2 (S2).[2] S1 is the initial scintillation light from the particle interaction inside the TPC. Recording this signal allows for the determination of the time and initial position of the interaction. S2 is the light from the electrons that drift to the EL region and produce the EL light. This signal allows us to record the energy of the event, which eventually is used in the reconstruction, calculation, and production of images. Moreover, the inclusive cut eliminates multiple S2 signals for any given event, an indication of simultaneous interactions such as a second decay, by establishing a cut-off of one S2 signal per event.[2]

The fiducial cut focuses on the active site of the TPC by limiting data recorded outside of the predetermined fiducial volume ($Z_{min} > 20$ mm, $Z_{max} < 510$ mm, and $R_{max} < 178$ mm). This cut allows us to ignore reconstructed events that start outside the fiducial volume and focus on events that start 20 mm within the outer surface, ensuring that the selected events are most likely not background events that began outside of the volume.[2] This cut also implements the previous inclusive cut.

The first topological cut is the single-track cut, which eliminates reconstructed events with multiple signal-like or discontinuous tracks. These signal-like tracks may also appear like a radioactive background that is eliminated by the previous cut algorithms. The next topological cut is the overlapped blob energy cut which eliminates events that have any overlapping blobs. The final topological cut is the blob energy cut, which calculates the energy and restricts events to the parameters of the size and shape of the event we are looking for.[2] First, the code finds the two endpoints of the track, then makes a 21 mm radius sphere, or blob, at each end point, calculating the total energy deposited in each blob.[2] The cut eliminates the reconstructed events where either of the blobs has a total energy less than the established energy-dependent threshold that is determined with this equation: $E_{thr} = A \times (1 - e^{-t \times E})$.[4] We are able to use this differentiation in energy between blob endpoints to eliminate single-electron events, which could be background events.

2.2 Comparison of Large and Small Opening Angles

The comparison of large and small electron opening angles was motivated by the blob energy and overlapped blob energy cut efficiency dependency on the opening angle as seen in Fig. 2. These two topological cuts were the only cuts affected by the true simulated angle between the two decay electrons leaving the nucleus. The comparison involved the reconstruction of the energy and tracks from the MC simulation of 3D events.


Figure 2. Measurement of cut efficiencies. The electron opening angle dependency can be observed by comparing the smaller angles' efficiency, with the lowest dropping to 60%, against the large opening angles', which reach nearly 80% in the blob energy cut. The same trend occurs in the blob overlap cut, but less dramatically. Nevertheless, the nonlinearity of the efficiency motivated the comparison of events where electron opening angles varied.

Since the dependency on the opening angle was detrimental to one of the cuts, we expected to find obvious distinctions between large and small opening angle events that could explain the higher amounts of failed events correlated to the small opening angles. However, no clear differences were found (see Fig. 3). For this reason, histograms plotting the number of events as a function of the energy fraction were created. These histograms established that large opening angles tend to have a higher energy fraction per electron, whether or not they pass the cut, while the small angle events have a smaller kinetic energy fraction. This explains why the efficiency is lower at smaller opening angles (see Fig. 2), since lower energy fractions indicate less energy for each blob. Both large and small angles pass both cuts with the same ratio (Fig. 4). However, a slight difference between the large and small angle events that passed the cuts can be seen; there are more "large angle" events that have a higher energy fraction. This shows that the electron's energy is more equally divided in half in large angle events. Because large angle events have a higher energy fraction, the electron energies are more equally split as a result of complicated nuclear mechanics.
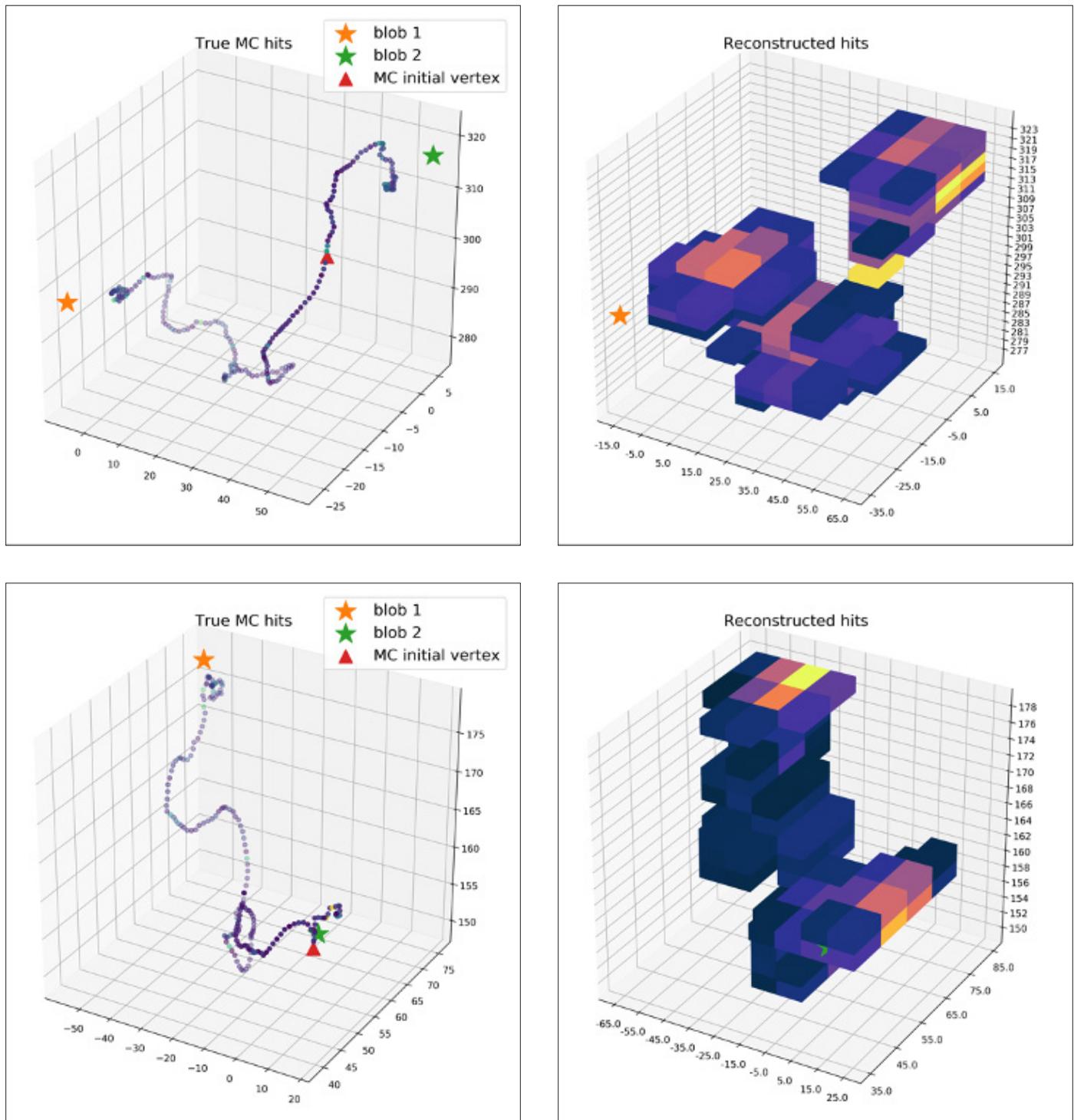
Figure 3. The original track (left) and voxelization (right) of events 178 (top) and 530 (bottom). Both 178 and 530 passed all five cuts, but with different opening angles. Event 178 was categorized as a large opening angle event, while event 530 was categorized as a small opening angle event. The voxelization of both events shown on the right demonstrate the blob and energy calculations. The darker colors signify lower energy deposits while the brighter colors signify higher energy deposits.
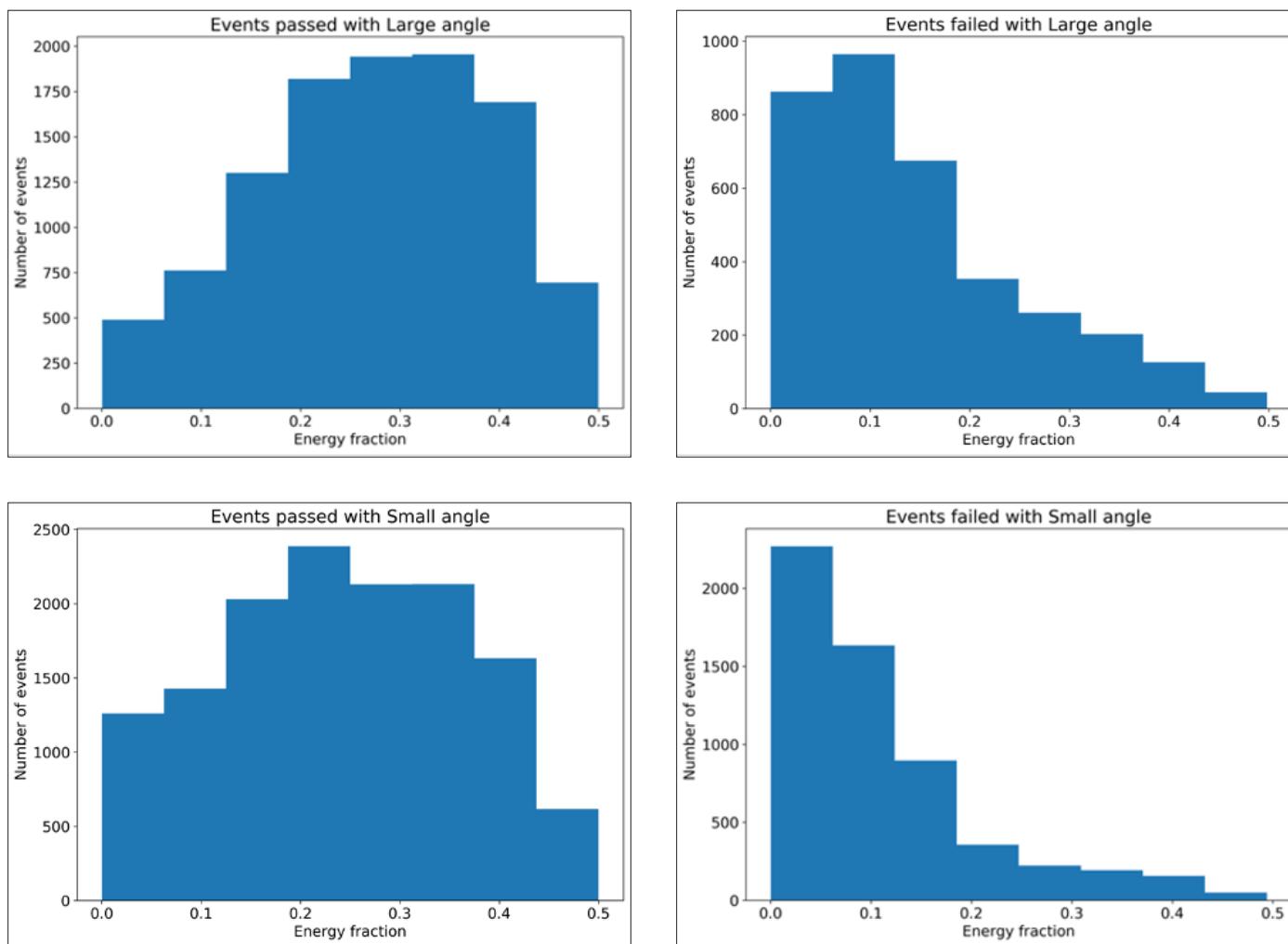
Figure 4. Data recorded for the events passed and failed with various opening angles. The histograms above illustrate the events that pass all five general and topological cuts. A large angle is defined as any event with an electron opening angle larger than 2.7 radians, and a small angle is defined as any event with an angle less than 1 radian. In other words, the two plots on the top contain only the events with a large opening angle, while the two on the bottom contain only events with small opening angles. All four histograms include all the data from the NEXT-White Monte Carlo simulations.

3. Results

3.1 Efficiency Plots

The constant efficiency throughout the various opening angles is shown in Fig. 5. The shift from green to yellow in the x-direction of the plot indicates the efficiency increasing as the kinetic energy fraction increases proportionally. However, the lack of a trend in the y-direction of the plot indicates the smallness of the effect the electron opening angle has on our efficiency cuts. This trend indicates that, if the nuclear physics model the NEXT collaboration used to simulate two-electron events has some uncertainties in the calculations of the opening angles, that uncertainty will not have a detrimental effect on whether those events are selected. Therefore, Fig. 5 corroborates the information presented in Fig. 2 since the efficiency cut falls flat as the opening angle increases. Those effects are discussed further in section 3.2.

3.2 Systematic uncertainties

The 2D efficiency plot in Fig. 5 shows that the opening angle will have little to no effect on our final measurements. This can be quantified. See Fig. 6, which demonstrates how moderately our results would change if our MC model incorrectly calculated the distribution by 10%. Fig. 6 was computed by reweighting all events by ±10%, thus varying the opening angle by 10% and creating the error bars that represent the uncertainty. Even though the uncertainty may seem generous, a 10% uncertainty is shown not to affect our model in any unfavorable manner.
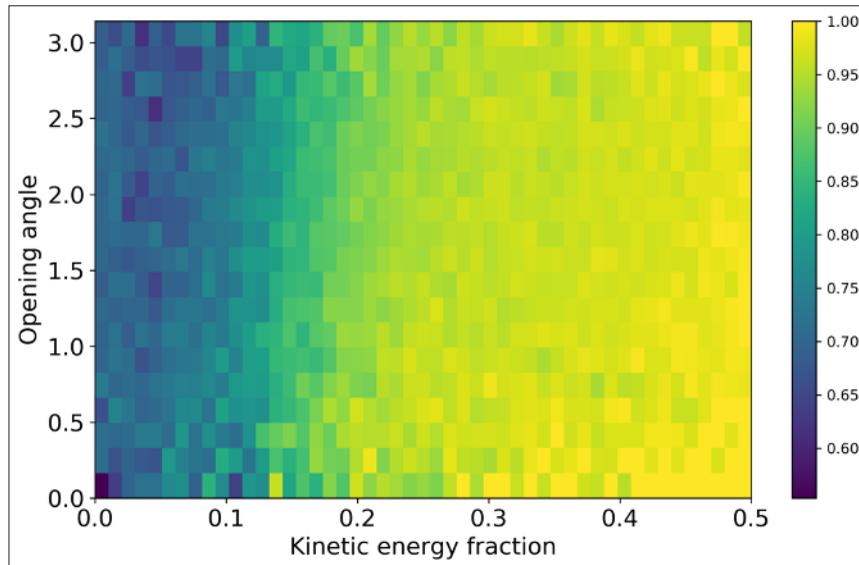
**Figure 5.** A 2D efficiency plot of the electron opening angle vs. the kinetic energy fraction. Brighter colors indicate a higher efficiency, darker colors indicate a lower efficiency.
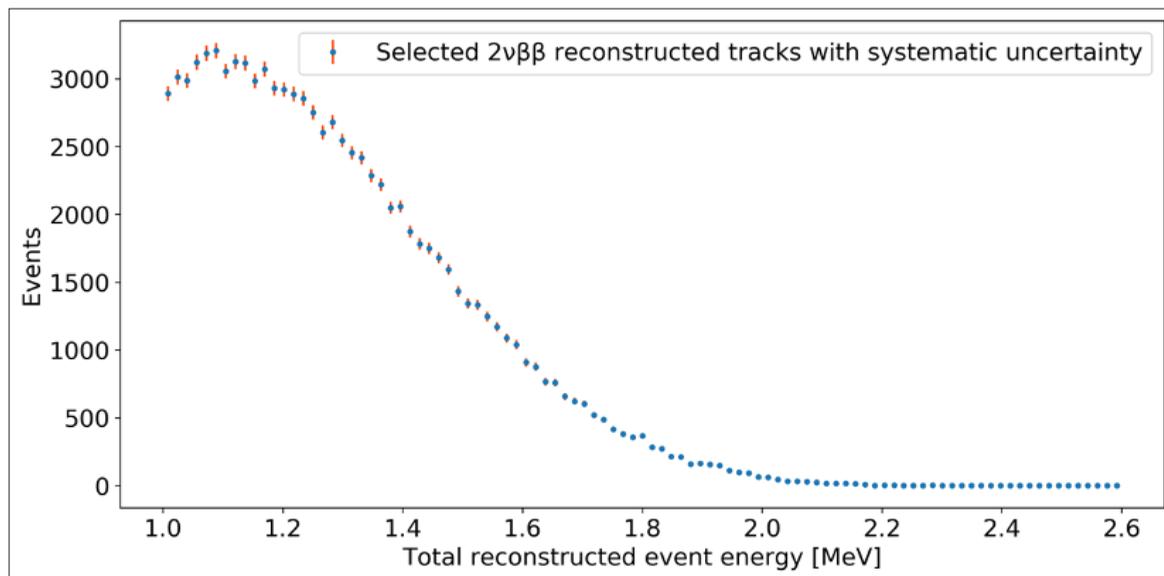
Figure 6. Systematic uncertainty measurements. The original data is represented by the blue data points, and the systematic uncertainty of the electron opening angles varied by 10% are represented by the error bars.

Fig. 7 supports this claim as it exemplifies how small the systematic uncertainty is, as a fraction of the total number of events, due to a change in the electron opening angle. Therefore, the potential mis-modeling at low energies (below ~ 1.8 MeV) may only have a systematic uncertainty of 0.1%, even with the mis-modeling being incorrect about the electron opening angle by as much as 10%. Moreover, the maximum uncertainty is ~ 2.5%, and that is a worst-case scenario at ~ 2.25 MeV.
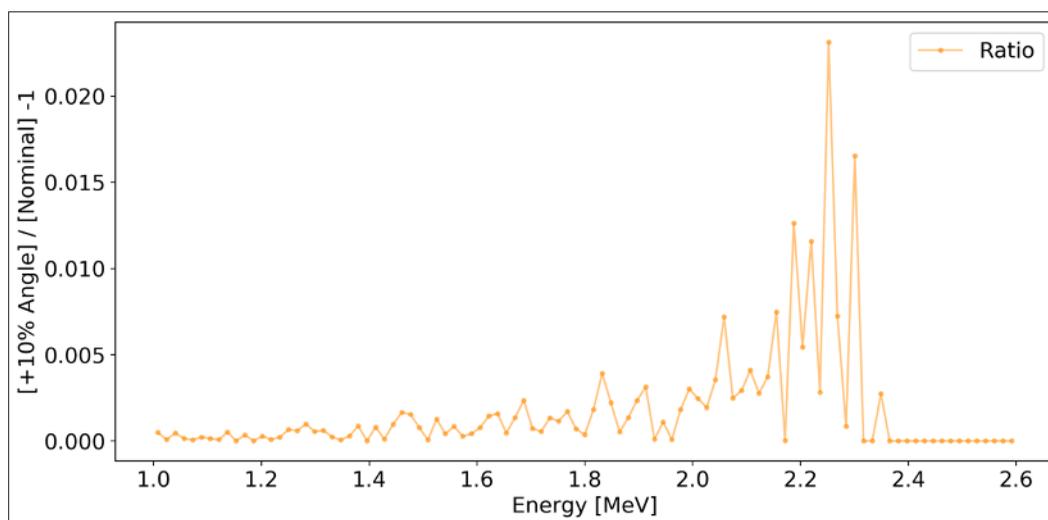
Figure 7. The variance of the effect caused by potential mis-modeling increases as the energies increase since there are so few events at those energies. This small pool of Monte Carlo simulation data increases the uncertainty as well. The points sitting at 0 are due to the lack of events in those energies.

4. Conclusion and Discussion

With the results of this thorough study, we can confirm an efficient reduction of 2νββ as a background. The recorded uncertainties procured from the simulation, reconstruction, and cutting of 2νββ has been observed to be exceedingly low. These findings are crucial. The nuclear physics model has been an elusive contributor to the uncertainty of largely unknown scale in detecting 0νββ. However, this study has served to somewhat quantify this scale, which further exemplifies the importance of these relatively low uncertainties. This advancement has established a systematic effect—albeit a low one—on the contamination of the onubb region of interest. Moreover, 2νββ events appear to be one of the most common background events in experiments like NEXT.[5] Therefore, the confirmation of low systematic uncertainties based on the electron opening angle is of significance, as the selection cuts have a low sensitivity to the variation of these opening angles.

Our collaboration still seeks to further investigate both the improvement of the selection cut efficiency and the future utility of the nuclear physics model. We intend to advance all five cuts in order to further improve total selection cut efficiency. This efficiency currently sits below 20% for the electron opening angle factor, and sits even lower for background events.[6] The further examination of the nuclear physics model calls for an investigation of how accurately it simulates, reconstructs, and cuts other radioactive background events such as thallium-208, bismuth-214, cobalt-60, and potassium-40.

Acknowledgments

References

1. V. Álvarez et al., "NEXT-100 technical design report (TDR). Executive summary." *J. Instrum.*, vol. 7, no. 06, 2012, https://doi.org/10.1088/1748-0221/7/06/t06001.

2. J. Renner, "Background rejection in NEXT using deep neural networks." *J. Instrum.*, vol. 12, no. 01, 2017, doi:10.1088/1748-0221/12/01/t01004.

3. ---. "First proof of topological signature in the high pressure xenon gas TPC with electroluminescence amplification for the NEXT experiment." *J. High Energ. Phys.*, vol. 01, no. 104, 19 Jan. 2016, https://doi.org/10.1007/JHEP01(2016)104.

4. NEXT Collaboration, P. Novella, et al., "MC Efficiency correction for double beta analysis," June 2020, internal collaboration document, https://next.ific.uv.es/DocDB/0010/001064/001/data_mc_eff_slides_june.pdf.

5. A. Gando et al., "Search for Majorana neutrinos near the inverted mass hierarchy region with KamLAND-Zen." *Phys. Rev. Lett.*, vol. 117, no. 8, 2016, doi:10.1103/physrevlett.117.082503.

6. K. Woodruff et al., "bb2nu_systematics," https://github.com/k-woodruff/bb2nu_systematics.

PERFORMING QUALITY CONTROL AND CHARACTERIZATION FOR PIXEL-BASED LARTPCS

Curtis Kizer-Pugh

Physics & Mathematics Major

Faculty Mentor: Jonathan Asaadi, Ph.D

Department of Physics

ABSTRACT

New technology in low-power data collecting and multiplexing circuits has allowed for the development of pixel-based liquid argon time projection chambers (LArTPCs). Pixel boards are expected to be orders of magnitude higher in resolution than contemporary wire-frame-based LArTPCs. Current wire frame detectors suffer from limitations reconstructing flight paths when they travel parallel to a wire frame or when placed in a high-flux environment, making them poorly suited as near detectors. Pixel-based detectors do not have these limitations, the LArPix collaboration plans to install a pixel-based LArTPC as a near detector at the Deep Underground Neutrino Experiment. Before installation, the detector boards must first be tested for quality control and characterization. The team at University of Texas at Arlington is tasked with developing both a test stand to house the boards and TPCs and a rigorous test procedure. Rigorous testing and characterization are necessary to ensure high-quality detectors and are part of the rapid development of new PixLAr boards. A test stand that can host multiple boards for simultaneous testing in a controlled environment has been designed and built. Likewise, a procedure for using the equipment necessary to test the boards has been developed.

1. Introduction

Neutrinos are one of the fundamental particles of the universe. Neutrinos are little understood because of their limited interactions with matter and their miniscule cross section. Neutrinos promise answers to fundamental questions about the universe; it is hypothesized that neutrinos may explain the matter-antimatter imbalance in the universe through their oscillatory nature and discrepancies between neutrinos and antineutrinos.

Due to their limited interaction, neutrino detection can pose a challenge. Neutrinos interact with atomic nuclei through the nuclear weak force, and a flight path can be reconstructed by detecting these interactions. Liquid argon time projection chambers (LArTPCs) have proven to be an excellent form of detector based on this principle. Liquid argon is a relatively dense, cost-effective medium. The density of the medium is proportional to the likelihood of an interaction. Furthermore, when excited by a neutrino interaction, argon becomes ionized by shedding electrons, which can be readily observed.

LArTPCs observe neutrino interactions indirectly through electron drift. The argon medium is exposed to strong electric fields, which induces movement in the electrons. The electrons are collected and the flight path of the neutrinos can be reconstructed. Current LArTPCs rely on wire frames to collect electrons. When the electrons reach one of the wires, its charge is collected and transmitted along the wire. By using multiple frames and measuring the time difference in charge read-outs, a three-dimensional flight path can be constructed.

Wire frames are not without issues, however. An incident particle traveling parallel to the wires in a wire frame creates ambiguity in the reconstruction, and a high incident rate can overwhelm the reconstruction effort. Because of this, along with their generally costly and fragile nature, wire frame TPCs are not ideal near detectors. Pixel-based detectors, however, do not suffer from these setbacks as they do not rely on wire arrays and provide much quicker readout.

Pixel-based readouts have seen success in gas-based TPCs, but new breakthroughs in cold, low-power preamps and data multiplexing have allowed for the development of pixel-based LArTPCs. The biggest limiting factor for a pixel-based detector is the number of data channels one is willing to accept. A pixel-based detector can have orders of magnitude higher resolution than a wire frame alternative, but at the cost of orders of magnitude more data channels. Any electronics used must also be sensitive yet low power. Power usage creates heat, which can affect the cryogenic environment of the detector.

Data multiplexing reduces the number of channels necessary by using a Fourier transformation to take the data from pixel space to frequency space, drastically reducing the number of channels necessary. Data can then, when desired, be returned to pixel space via the inverse Fourier transformation. A reduction in the number of I/O channels is not enough, however. Previous circuits consumed too much power, and, if used in a LArTPC, the heat generated would cause localized boiling of the liquid argon. A preamp has been developed, however, which is able to operate fully submerged without producing localized boiling.[1] A combination of these factors allows for the design and manufacturing of pixelated LArTPCs.

Pixel-based LArTPC demonstrations have shown the technology to be highly effective. Pixel-based LArTPCs are relatively low noise, an exciting prospect for the fine measurements sought after in neutrino physics. A 2018 collaboration demonstrated a signal-to-noise ratio of approximately 14 for commercially made pixel boards.[2] A similar collaboration later in 2018 produced data suggesting a potential signal-to-noise ratio of 55.[3] The data reconstruction offered by pixel-based systems is as exciting a prospect as the low-noise data. Pixels offer a 2D plane of collection while also measuring the time to collection, which in turn offers true 3D reconstruction, as opposed to the projective 2D reconstruction used with wire plane TPCs. Comparing the two methods in simulation implies a general superiority of pixel-based 3D reconstruction,[4] and, despite potential ambiguities from multiplexing, experiments seem to support the same conclusion.[3]

Due to their quick response time, low noise, and low ambiguity, pixel-based TPCs are ideal to act as near detectors for a neutrino beam. Furthermore, near detectors need not be as large as far detectors, meaning the size constraints placed on a detector by the number of channels is not as severe. To study neutrino oscillation with a minimum of variable factors, a near detector and a far detector would ideally be as similar to one another as possible. If proven successful as a near detector, pixel-based TPCs could be scaled into larger detectors with a modular design.[5]

A pixel-based LArTPC, known as ArgonCube, has been commissioned and is a candidate to be a near detector at the Deep Underground Neutrino Experiment (DUNE), the U.S. flagship for research in high energy physics. DUNE hopes to shine light on many unknowns about neutrinos, such as mass state hierarchy and the scale of CP-violation. Understanding these key unknowns about neutrinos may explain how the early universe was able to create an asymmetry of matter and antimatter, resulting in the matter-rich universe. Through the LArPix collaboration, consisting of the Lawrence Berkeley National Laboratory (LBNL), the University of Bern, the Fermi National Accelerator Laboratory, and the University of Texas at Arlington (UTA), a pixel-based detector board known as PixLAr has been developed for use in ArgonCube. Before it can be installed at DUNE, however, the new detector must go through many phases of development and testing. The team at UTA is responsible for QA/QC of PixLAr as well as characterization of the boards and providing hands-on feedback for further development if necessary.

Each PixLAr board must be tested for quality and to characterize its behavior. The boards will be submerged and tested in small scale TPCs, which use a high-voltage cathode to induce electron drift instead of a particle event. Each TPC will hold two PixLAr boards, sharing a cathode in common between them. Each board has 144 LArPix application specific integrated circuits (ASICs), each of which is responsible for 64 pixels.

The LBNL group is responsible for development of the LArPix chip, PixLAr boards, and scale TPCs. The team at UTA will use its cryogenic facility equipped with cryostats, a liquid argon filtration device, and a liquid argon purity monitor to test the boards in a purified liquid argon environment. To achieve replicability, increase efficiency, and minimize sources of error, a test stand and procedure to accompany it are necessary to develop.

2. Test Stand

The test stand's design posed a few considerations. The tests will be done in a cryogenic environment, and the materials used in the test stand must be able to tolerate the extremely low temperatures without significant thermal expansion or contraction. The environment is also one of highly pure liquid argon, and any materials used must not significantly outgas when exposed. The TPCs rely on high voltage to function, and thus conductive materials must be used sparingly and with a certain berth to the high-voltage components. Perhaps most importantly, the test stand must allow data collection; it should allow for ease of read out, must fit within the cryostat at UTA, and should allow for multiple TPCs to function at once. The TPCs as designed by the team at LBNL have a footprint of 334.78 mm by 92.78 mm and are to be spaced 7.2 mm apart. The UTA cryogenic facility uses a Cryofab CF3048-F cryostat with an inner diameter 755.14 mm. The LBNL group proposed testing five TPCs at one time, a total of 492.8 mm across, which presented a size limitation for the test stand as well. Finally, the stand should be able to house or support ancillary sensors (e.g., liquid level monitor), as well as providing bracing for cable management. The stand uses mechanical mounting, rather than chemical adhesives. Many epoxies will not function in or after exposure to a cryogenic environment, and while some epoxies are cryo-rated, chemical adhesion risks outgassing, which would degrade the purity of the liquid argon environment.
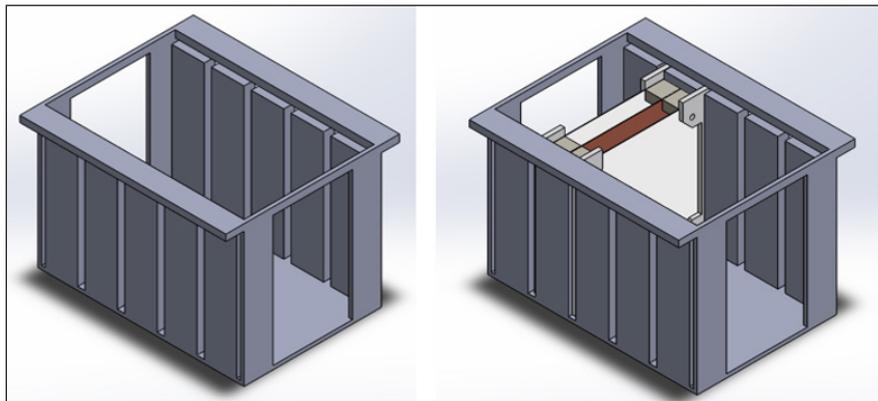
2.1 Test Stand Version 1

The first design pre-exists the TPC designs provided by LBNL. The design relies on sandwiching the PixLAr boards and cathodes between blocks with recessed cuts to hold them in proper positions. The brackets and blocks would hold the cathodes and boards at the appropriate distances apart, as well as the appropriate distances between, TPC units. The recessed cuts would be as deep as the printed circuit boards are thick, allowing them to be firmly secured, while also protecting the boards from overtightening. The TPC modules are designed to be attached to one another to form a coherent unit, which then could be seated into a slotted structure.
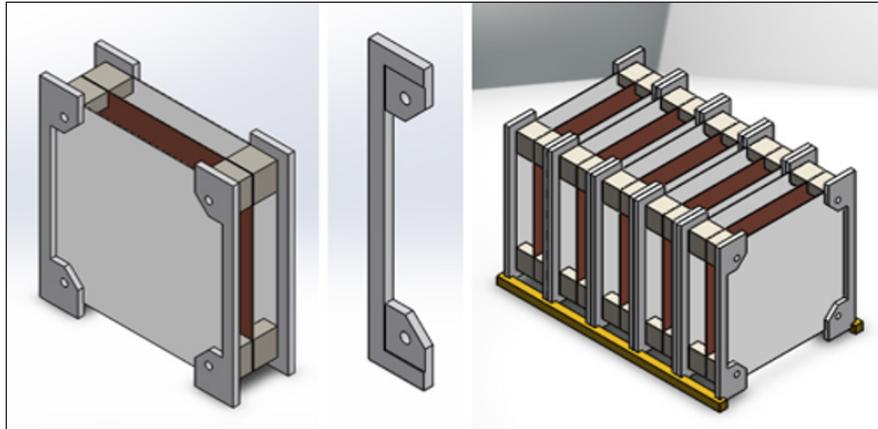
Figure 1. From left to right (all CAD models): an individual TPC module; one of the structural brackets demonstrating the recessed cut; a five TPC unit resting on a slotted base

2.2 Test Stand Version 2

The TPC modules of the first design were retained in the second. The idea of a coherent unit, however, was scrapped; we believed such an arrangement would be unwieldy and left the boards open and easily damaged. In the second design the TPCs would be inserted into a slotted basket, which would hold them in place. The slotted design would allow for the boards to be sandwiched without the need for fasteners.

Figure 2. From left to right (all CAD models): the basket model; the basket with a TPC module inserted, demonstrating the slotted design

2.3 Test Stand Version 3

The team at LBNL developed scale TPCs to facilitate testing their PixLAr boards, and thus many features of the previous test stand design became unnecessary. The basket, however, remained a design constant. Instead of being slotted to hold the TPCs in place, the test stand design took advantage of the TPCs top mounting holes and a spacing bar to keep them in proper placement and added walls between the TPCs. The basket was to be made of garolite, a composite fiberglass material that is nonconductive and cryo-friendly and is offered commercially in sheets of a variety of thicknesses. The design of the basket took inspiration in its construction from laser-cut wooden structures. The slotted design allows it to be held together in a mechanical fashion with tension provided by a series of rods running the height of the basket. The basket was expected to attach to the lid of the cryostat, which would have allowed the basket to be removed from the cryostat simply by lifting the lid. Unfortunately, the crane used at the cryogenic facility at UTA does not lift high enough to allow for clearance and so the idea of a lid mount was scrapped.
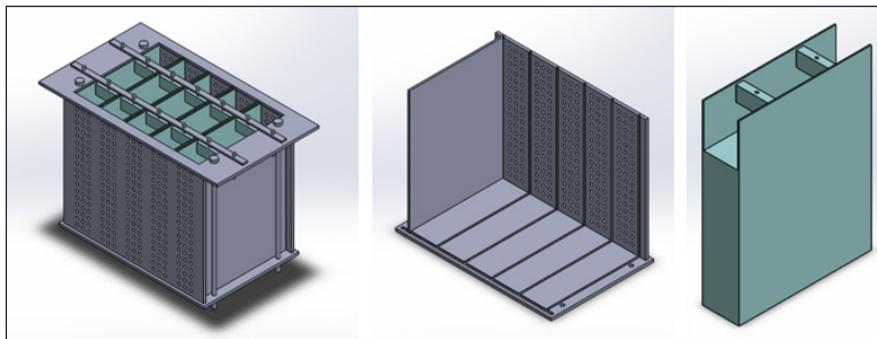
Figure 3. From left to right (all CAD models): a fully assembled basket with TPCs inserted; a basket with features removed to highlight its slotted construction; a low polygon count model of TPC design

2.4 Test Stand Version 4

Garolite is a durable material but can be difficult to machine. It requires hardened bits and lubrication, dulls cutting edges rapidly, and risks delaminating the sheets of fiberglass. Due to limited accessibility to mills capable of machining garolite and the complications it could lead to, we shifted the design away from a slotted construction in favor of a stainless-steel strut frame to hold garolite sheets in place and provide structure. Stainless steel was chosen because its thermal expansion and contraction is similar to that of garolite.
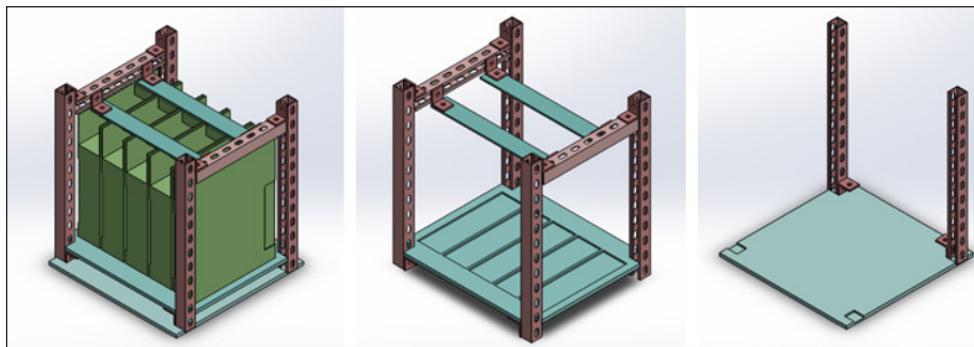
Figure 4. From left to right (all CAD models): the basket with TPCs installed; the basket with TPCs removed to show their slotted base; the shelf base with features of the basket removed to show the slots in which the frame rests

Instead of a structure attaching to the lid of the cryostat, a shelf would be placed at the bottom of the cryostat. The shelf is a square of garolite with diagonal lengths the same as the interior diameter of cryostat to provide four points of contact and increase stability. The shelf has four recessed cuts for the legs of the strut frame of the basket, intended to give the basket a stable footing and a set position in the cryostat for repeatability.

The base of the basket has recesses in which the TPCs rest, along with a bracing bar across the top as in previous designs. The rails of the strut allow for the fasteners to be loosened and the brace moved or removed for ease of access to the TPCs. The garolite pieces are attached to the strut frame by stainless steel brackets. The strut frame also acts as a point of contact for the crane to lift it out of the cryostat and as an attachment point for sensors or cable management.
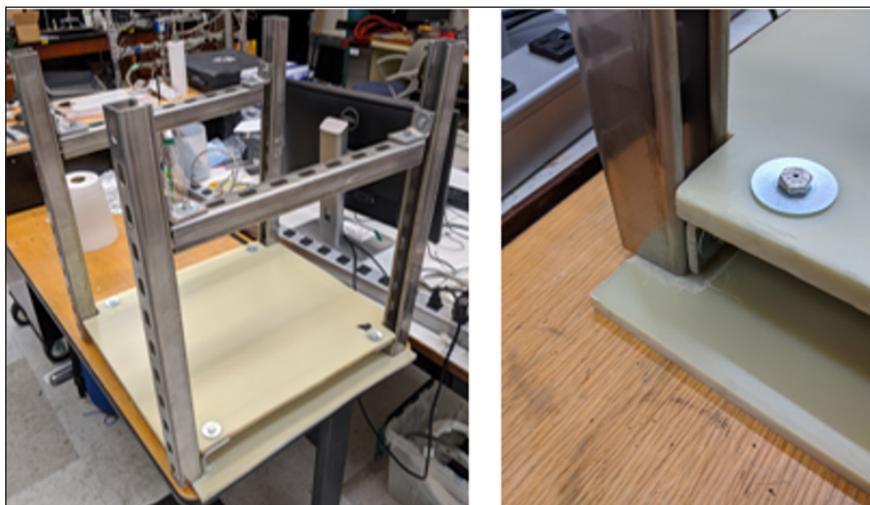
Figure 5. From left to right: the basket, minus the TPC bracing, resting atop the shelf; a corner of the basket frame resting in a recess in the shelf

The base shelf is a 24 inch by 24 inch by 0.5 inch thick sheet of garolite. Near each corner is a recess for basket alignment and stability which was ground into place using a rotary grinder on a Dremel tool. The base of the basket is a 21.5 inch by 18.5 inch by 0.5 inch thick garolite rectangle with a 1.625 inch square removed from each corner for the strut frame. The strut has a 1.625 inch by 1.625 inch footprint, so the basket as a whole has a 21.5 inch by 18.5 inch footprint. The frame of the basket is made of four 24 inch and two 18 inch strut segments. The assembly is completed with L-brackets, nuts and bolts, washers, and compression washers. The TPC bracing bars and TPC footprint recesses are not pictured. The team has elected to postpone their correction pending the delivery of the TPCs. Having the TPCs on hand is necessary to ensure placement and alignment.

3. Quality Control and Characterizing Logistics

Before their permanent installation and use, the pixel boards must be tested for functionality. They must also be characterized for noise and behavior. Characterization will provide feedback to the boards' developers at LBNL, which is key to the rapid development planned by the collaboration. The team at UTA is to develop a procedure to fully clean, test, characterize, and ship the boards.

The procedure is divided into stations, ideally to allow a workflow similar to an assembly line. Some tasks will take less time to complete than others, potentially creating a logistical backlog. The continued COVID-19 outbreak at time of research, however, may result in less of a backlog and more of a queue. Proper

safety will limit the number of people in the lab at one time and keep them separated by at least six feet, which will effectively limit the available labor for this project. Furthermore, work can be done in batches of ten, since the test stand holds five TPCs at a time. By batching and queuing, we hope the system will achieve high efficiency despite external complications.

3.1 Unpacking and Operational Tests

The pixel board and requisite test TPCs are to be shipped to UTA. The boards are fragile and can be damaged from errant static discharge, necessitating careful packaging. Upon arrival the boards should be brought to the lab, removed from their shipping containers, and organized into batches of ten. They should be left in static-protective containers until they are needed. It may be necessary to ground oneself with an antistatic wristband before handling pixel boards as added protection from static discharge.

Working a batch at a time, the boards must first be visually inspected for damage from shipping, making sure all electronic components are firmly attached, that there are no cracks in the soldering, that the traces are intact, and that there are no shorts in the traces. A magnifying lens may be necessary for a clear view of the smaller components and traces. Once the boards are visually inspected, they should be thoroughly cleaned with ethanol with special care given to the collection pads.

Once cleaned, boards should be tested for functionality. Testing the batch one board at a time, power the board with 5 volts DC and attach a computer to it via the ethernet port. If the board is functional it should show under the local network of the computer and can be accessed via SSH using the password *altisidora*. Once communication has been established, one can send commands to and receive data directly from the LArPix ASICs.

One can manually enter commands to the ASIC to check the functionality of the chips, but this is slow and inefficient. Another member of the UTA team is developing a python script based on the LArPix python libraries to perform these tests more efficiently. Once the boards are finished being tested, they should be sent to the next station for assembly. If the assembly station is not ready for them, they should be stored in a clean environment, free from dust and static.

3.2 TPC Assembly

Boards are to be attached to the walls of the TPCs via the screw holes. It will likely be more efficient and user friendly to partially (or fully) disassemble the TPCs, attach the boards to the walls of the TPCs, then reassemble the TPCs. The assembled TPCs should then be put into slots in the basket and fastened in place. Once the TPCs are in place, high voltage cables should be attached to the cathodes and the I/O cables should be attached to the boards. They should be routed up along the strut frame and zip tied in place.

The basket should then be lifted by crane and lowered into the cryostat. The basket rests atop a garolite base installed in cryostat. The crane should then be used to lift and hold the lid of the cryostat above to allow cables to be attached to passthroughs. Communication through the passthroughs should be tested before the lowering the lid. Once verified, the lid can be lowered and attached to the cryostat.

3.3 Cryogenic Operations

Once the lid is fully attached a vacuum is pulled on the cryostat. A vacuum is necessary to ensure the purity of the liquid argon environment. However, if a low enough vacuum is not feasible the system can be flushed with argon gas instead.

The purity of the liquid argon is monitored using an ICARUS style argon purification monitor.[6] Molecular sieves are used to filter liquid argon and remove contaminants. For the molecular sieves to filter contaminants

out of the argon, they must first be decontaminated themselves, a process called filter regeneration. The filters will outgas contaminants when heated and held in a vacuum.

The sieves used at UTA are heated to approximately 120 degrees centigrade by heating tape and held in a vacuum on the order of 10-5 to 10-6 Torr. After a few hours, the sieves will have outgassed most of the contaminants, mostly water and oxygen. To ensure the contaminants are fully removed, the system is monitored by a residual gas analyzer while flushed with a gas mixture of 95% hydrogen, 5% argon. The gas flow ensures the entire system has been completely evacuated of contaminants. Liquid argon can then be flowed through the sieves to purify it and then into the cryostat.
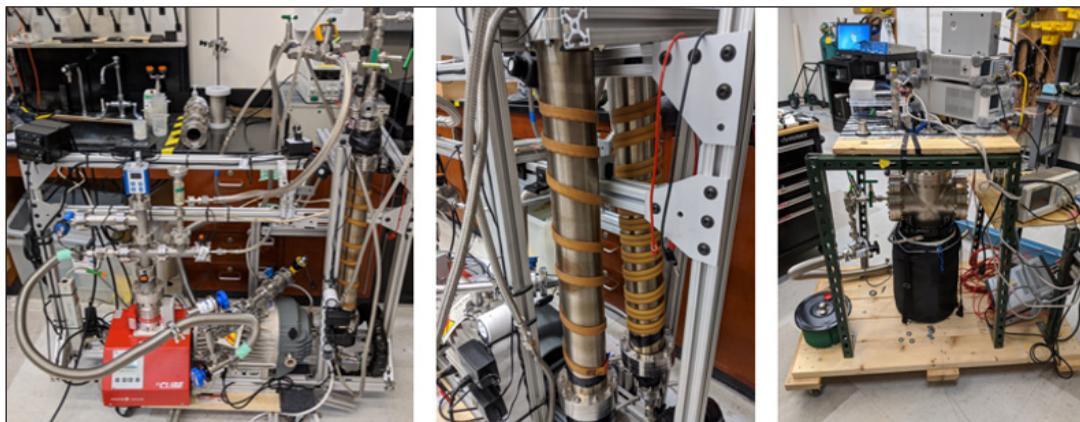
Figure 6. From left to right: The purification station self-contained on a cart; the molecular sieves of the purification station wrapped in heating tape; the liquid argon purity monitor on a cart

The cryostat is to be filled with enough liquid argon to fully submerge the TPCs. The volume of liquid argon in the cryostat is monitored using resistive thermal detectors and a capacitive liquid level monitor. All onboard electronics will be controlled by a dedicated Raspberry Pi.

3.4 Data Acquisition

Once the boards are fully submerged in a pure liquid argon environment, they are ready to be tested and characterized. Data acquisition is controlled by a Raspberry Pi using the LArPix python libraries. The libraries are available for both python2 and python3. The differences between them are minor, mostly relating to support lifetime. Raspian, the Raspberry Pi operating system, is Debian based, which does not support all the prerequisite packages for the python3 version of the libraries. The data acquisition and visualization scripts for the Raspberry Pi are still under development.

The high-voltage cathode will be turned on and the boards will be set to collect data over a given time. The collected data will then be compared with simulations to establish performance. It will be necessary to visualize data per channel or region of interest to identify any faulty components and to fully characterize each channels' performance and noise over a band of operational voltages.

3.5 Disassembly and Repackaging

Once the requisite data is collected, the cryostat is to be drained of liquid argon or given time to allow it to boil off. Once the system is warm, the lid of the cryostat is to be detached and lifted to allow cabling to be detached from the feedthroughs. The lid is then to be set aside and the basket lifted out of the cryostat. The TPCs are to be removed from the basket and the boards removed from the TPCs.

As the components warm up from cryogenic temperatures it is not uncommon for moisture due to condensation from the air to collect on surfaces. Components are to be dried and cleaned again with ethanol. The empty TPCs are to be sent back to the assembly station and the boards are to be organized based on performance, labeling any that act out of the norm. The boards should be stored in a clean, static-free environment until they are ready to be shipped. They should be packed for shipping with plenty of padding and with static protection.

4. Conclusion

Pixel-based readouts are the future in any projection chamber detector. Pixels offer orders of magnitude higher resolution over wire frame contemporaries, such as those used in LArTPCs. Advances in low-power preamps and data multiplexing have allowed the development of pixel-based LArTPCs using PixLAr boards. The team at UTA has been tasked with develop a testing procedure and test stand for the boards.

A test stand has been developed to work with the cryostat at the UTA facility. The UTA facility is also equipped with a liquid argon purification system and a liquid argon purity monitor. The boards will be tested and characterized in a series of stations acting in an assembly line. The assembly line relies on queueing heavy workload during periods of low activity due to the pandemic-imposed limitations on available labor.

As of writing the United States is facing an ongoing COVID-19 outbreak, which has posed issues to the research. Safety protocols limited the available staff and greatly delayed progress. The LArPix collaboration is, in part, made up of universities, which halted in-person work for some time after the initial outbreak. The UTA team had hoped to complete the quality control and characterization, but the boards and TPCs had not arrived. The project is still active, however. A test stand has been developed and assembled, as has a testing procedure, and the UTA team is poised to start as soon as the boards are received.

Acknowledgments

References

1. G. de Geronimo et al. 'Front-End ASIC for a Liquid Argon TPC'. In: *IEEE Transactions on Nuclear Science* 8.3 (June 2011), 1376–1385. ISSN: 0018-9499. https://doi.org/10.1109/TNS.2011.2127487

2. J. Asaadi et al. 'First Demonstration of a Pixelated Charge Readout for Single-Phase Liquid Argon Time Projection Chambers'. In: (2018). arXiv:1801.08884 [physics.ins-det]

3. D. Dwyer et al. 'LArPix: Demonstration of Low-Power 3D Pixelated Charge Readout for Liquid Argon Time Projection Chambers'. In: (2018). arXiv:1808.02969 [physics.ins-det]

4. C. Adams et al. 'Enhancing Neutrino Event Reconstruction with Pixel-Based 3D Readout for Liquid Argon Time Projection Chambers'. In: (2020). arXiv:1912.10133v2 [physics.ins-det]

5. M. Auger et al. 'A New Concept for Kilotonne Scale Liquid Argon Time Projection Chambers'. In: (2019). arXiv:1908.10956 [physics.ins-det]

6. S. Amoruso et al. 'Analysis of the Liquid Argon Purity in the ICARUS T600 TPC'. In: *Nuclear Instruments and Methods in Physics Research Section A: Accelerators, Spectrometers, Detectors and Associated Equipment*, 516.1 (2003), 68–79. https://doi.org/10.1016/j.nima.2003.07.043

MCNAIR ABSTRACTS

SUMMER RESEARCH

Exploring Formation of Carbon Structure in Silicon Oxycarbide Ceramics

Eman Alasadi

Chemistry and Physics Major

Mentor: Peter Kroll, Ph.D.
Department of Chemistry and Biochemistry

Polymer-derived silicon oxycarbide (SiCO) ceramics exhibit several outstanding properties and are considered for applications as functional ceramics in additive manufacturing and for energy storage. A key feature of SiCO materials is the so-called free carbon content, which are carbonaceous segregations embedded within an amorphous glass matrix. Properties of the material depend on the amount of carbon in the material as well as its actual distribution or morphology, that is, in how the carbon atoms are connected with one another and in the way they are embedded within the surrounding glass matrix. In this study, we use molecular dynamic simulations with an empirical potential (Tersoff type) to explore formation of carbon structures in SiCO. Our simulations mimic pyrolysis of the polymeric precursors and annealing of the amorphous ceramic at high temperatures. We model different annealing procedures, apply different heating and cooling rates, and realize structures comprising distinctly different carbon morphologies. We find that isolated carbon atoms of a molecular precursor are initially well dispersed throughout the material. Upon annealing they combine to larger, but finite segregations, which resemble polyaromatic hydrocarbons or fragments of single-layered graphene. These layered carbon segregations act like walls and effectively separate the surrounding amorphous matrix, essentially confining it in small domains. Continuity and sizes of these domains are related to the amount of free carbon and to the composition of the material. Above a certain temperature annealing yields formation of tubular carbon structures, which ultimately convert into large graphitic segregations.

Microbubble-Based Drug Delivery Systems for Treatment of Peripheral Artery Disease

Ahmed Gure
Biomedical Engineering Major

Mentor: Kytai T. Nguyen, Ph.D.
Department of Bioengineering

Peripheral artery disease (PAD) is caused by atherosclerosis plaque and obstructs peripheral arteries, blocking the blood flow to lower body parts and causing pain and numbness. This disease affects more than 200 million people worldwide and often occurs in elderly patients. Surgery is not a treatment option, while other conventional therapies, including medicine and gene therapy, have failed to achieve therapeutic efficacy. Ultrasound contrast agents such as microbubbles are emerging as an important tool in drug and gene delivery as well as in imaging detection of various diseases. In this project, we investigated on the fabrication and characterization of microbubble-based drug delivery systems to deliver oxygen and proangiogenic molecules for a combinatorial PAD treatment to overcome limitations of conventional therapies. We successfully fabricated oxygen-loaded microbubbles conjugated with dye-encapsulated liposomes as a model drug delivery system. This system consisted of an average size of ~2μm and was stable. In addition, screening of various proangiogenic molecules using angiogenesis studies found deferoxamine to be a potential candidate suitable for PAD treatment. Future work will focus on both in vitro and in vivo testing of our designed microbubble-based drug delivery system for delivery of oxygen and deferoxamine to effectively treat PAD.

State Assessment of English Language Arts Neglect Established Standards

Helen Hernandez
English Major

Mentor: James Warren, Ph.D.
Department of English

English Language Arts (ELA) educators and researchers maintain that high school students must develop rhetorical awareness to be college and career ready. An essential component of rhetorical awareness is the recognition that written communication does not target all readers but rather specific audiences. Despite the professional consensus that students should adapt their writing to specific audiences, there is reason to believe that the move in public education toward state content standards and large-scale standardized tests has resulted in students not learning the rhetorical flexibility required to adjust to different audiences. In this study, we examined the state content standards for ELA and the state-mandated writing tests for high school students in all 50 states and the District of Columbia. We found that while all states have adopted standards that require students to write for specific audiences, only a small percentage test this skill on state-mandated assessments. We argue that the consequences of this misalignment between standards and assessment are potentially severe. Since teachers often narrow the curriculum to content that appears on state tests, it could be that the majority of high school students across the United States are not learning that effective writing must be adapted to specific audiences.

Development of Methodology and Software to Ensure the Quality Performance of the Deep Underground Neutrino Experiment High Voltage Field Cage

Archit Jaiswal

Physics and Computer Science Major

Mentor: Jaehoon Yu, Ph.D.
Department of Physics

The Deep Underground Neutrino Experiment (DUNE) is the U.S. flagship experiment being designed to study the characteristics of neutrinos, which make up a quarter of the fundamental particle map. These subatomic particles help physicists understand the fundamental constituents of matter in the universe. In DUNE, neutrino interactions will be captured inside the active volume of the time projection chamber using liquid argon as the medium. The DUNE detector will be built using various parts assembled according to the proposed design in order to accomplish the precision measurements for the underlying physics goals. The basic parts of the detector are from various hardware manufacturers. It is crucial to ensure the quality of every component before it is assembled into such a gigantic structure, because a minor imperfection could compromise precision and cause significant uncertainties to the scientific measurements. In this research, a methodology and a software tool to conduct the quality assessment of the DUNE high voltage components, after the parts are delivered from the manufacturer, are developed. The outcomes of this research will be used to conduct quality assurance and quality control for all the high voltage parts before using them to build the components of the detector.

Donor Relation Communication:
A Case Study in Higher Education

Dallas Johnson
Communication Major

Mentor: Karishma Chatterjee, Ph.D.
Department of Communication

This study examines how major-gift officers use stewardship practices in university fundraising with major-gift donors. Geah Pressgrove's stewardship strategies, articulated in "Development of a Scale to Measure Perceptions of Stewardship Strategies for Nonprofit Organizations" (2017), were used as a theoretical framework. Semi-structured interviews were conducted with nine major-gift officers across various development offices and academic units in a large southwestern university to learn about the use of stewardship practices and interpersonal relationship building. Study findings suggest major-gift officers employ the following stewardship strategies to initiate and cultivate relationships with donors and stakeholders: reporting, regard, relationship nurturing, recognition, and responsibility. Face-to-face communication is considered the best medium to initiate relationships with donors. Participants indicated they individualize the medium of communication based on the preferences of the individual donors. Donors are thanked in a variety of ways, although thanking each donor at every level on a regular basis could be improved. Interpersonal interaction is considered to be key to helping prospective donors realize their passion and connect to university initiatives. The study was able to conclude the importance of the use of communication, particularly interpersonal communication, to build and maintain relationships with donors in the higher education field. Regular communication practices that deploy stewardship strategies are essential for donor giving of time, talent, and treasure.

Dynamic Analysis of a Hexapod Robot on Uneven Surfaces Using AUTOLEV and MATLAB

Ephrem Kejela

Aerospace Engineering Major

Mentor: Alan Bowling, Ph.D.
Department of Mechanical and Aerospace Engineering

This paper discusses the dynamic model of a hexapod robot's leg using AUTOLEV and MATLAB programs. In addition, the documentation of the AUTOLEV program is presented to model a hexapod robot. The development of the model follows a systematic approach. This systematic approach addresses two aspects of mechanics—kinematics and dynamics. The kinematics aspect of the documentation looks at motion without considering the forces that cause it. Kinematics describes motion in terms of position, orientation, velocity, and acceleration. The dynamics aspect of the documentation considers the forces that cause movement, including forces and moments that lead to the equations of motion of the hexapod robot. These kinematics and dynamics aspects of the hexapod's movement steps were coded into a software to make the hexapod model. AUTOLEV is used to model and control the hexapod's performance in interacting with the environment. In these first steps, the equations of motion of the hexapod robot's leg were generated using AUTOLEV. Also, a general MATLAB simulation code based on user input was generated through AUTOLEV. The development of contact and control algorithms begins with modeling the hexapod robot using AUTOLEV.

Regulation of Cell Wall Synthesis in Mycobacteria

Heather Lake
Biology Major

Mentor: Cara Boutte, Ph.D.
Department of Biology

Mycobacteria are a genus of bacteria that includes the causative agent of Tuberculosis. Due to the unusual growth pattern and cell wall of Mycobacteria, their regulatory processes for division remain largely undiscovered. The regulation of cell wall enzymes in the division process, for example, remains unclear. Cells must have regulatory enzymes to ensure that cell wall enzymes are working in such a way to avoid cell lysis. One such putative regulator that is known to be involved in cell division in Mycobacteria is SepIVA. In the absence of SepIVA, cells are unable to divide, leading to lengthened cells. In preliminary microscopy data, it seems that there are changes in the localization patterns of the cell wall enzyme MurG when SepIVA is conditionally depleted in the cell, with cells depleted of SepIVA forming sporadic localizations throughout the cell rather than being uniformly distributed. This indicates there may be some unknown relationship between the SepIVA protein and MurG localization in M. Smegmatis.

Mechanistic Studies of F420-Dependent Glucose-6-Phosphate Dehydrogenase Using X-Ray Crystallography

Charlene Mandimutsira
Biochemistry Major

Mentor: Kayunta Johnson-Winters, Ph.D.
Department of Chemistry and Biochemistry

F420-dependent enzymes play important roles in numerous biological processes. F420-dependent glucose-6-phosphate dehydrogenase (FGD) catalyzes the conversion of glucose-6-phosphate to 6-phosphogluconolactone, which is important within Mycobacterium tuberculosis (Mtb) and Nocardia. Until our work, these enzymes, in general, have not yet been subjected to rigorous enzymological investigation. We have unraveled several key pieces of information concerning the hydride transfer mechanism of FGD. However, it is still unclear as to where the substrate, glucose-6-phosphate (G6P) binds within the active site of FGD, which can be determined through x-ray crystallography of an inactive FGD variant. Two previous FGD crystal structures were solved, one from Rhodococcus jostii RHA1 I 2017 and the other from Mtb, in 2008. The Mtb-FGD structure was solved in the presence of citrate, which is a competitive inhibitor of the enzyme with respect to G6P. The goal of this project is to grow crystals using an FGD-substrate or FGD-substrate analog complex with conditions that exclude citrate. To prevent turnover, we propose to synthesize the G6P analog, 1,5-anhydro-D-glucitol 6-phosphate. We are optimizing crystallographic conditions in order to produce high resolution protein crystals using screens from Hauptman Woodward Medical Institute. Favorable candidates will undergo x-ray diffraction to determine the resolution.

Improving Public Health Initiatives with Social Science: Lessons Learned from COVID-19

Paola A. Puentes

Anthropology and Biology Major

Mentor: Shelley L. Smith, Ph.D.
Department of Sociology and Anthropology

While epidemiological modeling studies show that nonpharmaceutical interventions have been effective overall in deterring the spread of COVID-19, contagion continues in many nations. Sole implementation of public health interventions may not be enough to end the spread of COVID-19. In my research, I demonstrate the value of social science in the field of public health and how it can help fight the current pandemic. Published literature from studies conducted in Malaysia, China, Vietnam, Uganda, and the US reveals predictors of human behavior during the current health crisis. Survey results show that knowledge levels and attitudes affect public adherence to health recommendations. Those least informed and least optimistic about COVID-19 were found to be less likely to wear a mask, practice social distancing, and practice enhanced hand hygiene across multiple studies. Additionally, I suggest fatalism and mistrust in science may also be contributing to nonadherence to health recommendations by the public. Increased research on the social dimensions of the COVID-19 pandemic can reveal demographics that may benefit from targeted health communications. Interdisciplinary research between the social sciences and public health agencies holds real promise in improving effectiveness of health campaigns across the world and impeding further spread of COVID-19.

An Analysis of the Metastatic Capabilities and Drug Resistivities of Patient-Derived Brain Cancer Cells

Anthony Sajik Ruiz

Biomedical Engineering Major

Mentor: Young-Tae Kim, Ph.D.

Department of Bioengineering

Glioblastoma multiforme is one of the most aggressive forms of stage IV astrocytomas, which comprise a significant portion of all primary brain tumors diagnosed in cancer patients. Different experimental methods and models have been utilized to analyze the fundamental characteristics of cancer cells; however, continuous research has revealed the necessity for a deeper examination involving the metastatic processes and the acquired changes in morphology pertaining to migrating cancer cells. Specifically, the onset of drug resistance following delivery of cancer killing agents on migrating cancer cells. In this study, polydimethylsiloxane microchannel devices were designed to imitate and facilitate physical confinement during the migration of glioblastoma cells in a 3D microenvironment. Patient-derived cancer cell lines (G55, C24, C25, C61, and C63) were tested to measure their viability via MTS assays involving 2D and migratory forms of the cancer cells treated with a cancer killing drug, temozolomide, under physical confinement. All brain cancer cell lines expressed the essential migratory capabilities through the experimental polydimethylsiloxane devices. Ongoing testing has shown that certain migrating cancer cells have had an increase in cell viability and consequently an increase in drug resistance to temozolomide. Current testing may reveal more information on the additional cell lines and their capabilities.

Divalent Cations Mediate Bacterial Tolerance to Carbapenems via Outer Membrane Stabilization

Richard D. Schargel

Biology and Microbiology Major

Mentor: Joseph Boll, Ph.D.
Department of Biology

Antibiotic tolerance remains a growing, yet understudied, problem in modern health care settings. Tolerant bacteria survive in otherwise lethal antibiotic concentrations. When the antibiotic is removed, tolerant bacteria resume normal growth. Similar to well-studied antibiotic resistance mechanisms, bacterial tolerance contributes to widespread treatment failure. However, the molecular factors that regulate antibiotic tolerance are not well understood. Antibiotic tolerance depends on the strain-to-strain variation as well as the administered antibiotic. Upon exposure to "last-line" carbapenem β-lactam antibiotics, tolerant gram-negative bacteria form spherical morphotypes devoid of a peptidoglycan cell wall. These morphotypes are commonly known as spheroplasts; furthermore, the molecular mechanisms and factors that mediate antibiotic-induced spheroplasts are mostly unknown. In this study, we examined the role of divalent cations on the outer-membrane of drug-tolerant bacterial spheroplasts in order to find an explanation for their ability to continue causing infection despite lacking a fundamental cellular component, the peptidoglycan cell wall. We found that spheroplasts are naturally fragile when cultured in Luria broth (LB) media, suggesting the presence of a stabilizing component in human serum that may promote antibiotic treatment failure. Spheroplasts in heat-inactivated serum have decreased permeability and increased survival relative to LB. We propose that divalent cations support antibiotic tolerance outer membrane stabilization, which decreases permeability and increases survival when exposed to physiological concentrations of calcium and magnesium.

Reactive Molecular Dynamics Simulations of Thermal Decomposition of Polysiloxanes

Thao-My Tran

Chemistry Major

Mentor: Peter Kroll, Ph.D.
Department of Chemistry and Biochemistry

Silicon oxycarbide is a type of porous ceramic with many desirable qualities such as high surface area, thermal insulation, and hardness. This material can be applied in a variety of fields ranging anywhere from drug delivery to circuit insulation. Pyrolysis of the polysiloxane polymer is one method used to synthesize silicon oxycarbide. With polydimethylsiloxane (PDMS) as the chosen polymer precursors, we are doing a preliminary test of the pyrolysis of PDMS through molecular dynamics using the reactive force field. Reactive force field is a bond-order-based force field that allows for a greater understanding of the system's chemistry and longer simulation time. From the simulations, one can detect a variety of chemical reactions including the rearrangement of methyl groups into the polymer backbone forming bridging—CH_2—units, the formation of mixed tetrahedral units SiC_nO_{4-n} (n=0,1,2,3,4), and the evolution of gaseous species as well as methane gas. Moreover, one can also observe segregation of carbon into aromatic units and the early stage of the precipitation of grapheme in these materials.

Impact of Need for Cognitive Closure on Framing

Omar Yanouri

Biology and Psychology Major

Mentor: Daniel Levine, Ph.D.
Department of Psychology

Need for cognitive closure (NFCC) is an individual's tendency to dislike ambiguity and prefer concrete solutions. Prior literature shows that, in simple situations, the trait leads individuals to employ cursory information acquisition and superficial judgements. However, NFCC may lead participants to consider a problem and surrounding information more thoroughly when it is challenging or understood to be important. This study tests the hypothesis that NFCC may lead to an increased susceptibility to framing effects and that the trait will interact with an elaboration prompt to reduce framing effects among those high in NFCC. Results show NFCC did not affect participants' susceptibility to framing. However, in the negative problem frame respondents with high NFCC displayed a reduction in framing effects.